

Appendices

Appendix A

Analysis tools

We introduce the measures that are being used extensively throughout the thesis. Standard measures such as gyration tensor, radial distribution function, velocity autocorrelation function, and mean squared displacement are mentioned from the practice point of view. We also mention the procedure of applying the shape matching order parameter. The details in these analysis tools can easily be found from molecular simulation textbooks and the literature.

A.1 Standard measures

A.1.1 Clustering

In assembled structures such as body-centered cubic micelles, hexagonally packed cylinders or lamellar phases, it is desired to identify separated clusters of nanoparticles (NPs) from which local structural properties, for example, the number of NPs per cluster, or the cluster geometry, center of mass, chirality and helicity, can be extracted. A cluster is defined by a cutoff distance within which the NPs (and their constituent beads) are adjacent neighbors.

Given the Cartesian coordinates of the beads under consideration (e.g. of a specific type or in a specific region of the box), the naive clustering algorithm implemented in this thesis involves a recursive function which loops through the neighbors of every bead and adds the beads to the current cluster. Once counted to a cluster, the beads are considered visited. The recursive function returns when all the beads are visited. Note that the beads in a cluster should be sorted by their index to ensure that the beads belonging to an NP are consecutive. In certain cases, the NPs in clusters should also be sorted by their distance to a fixed location in space (e.g. for calculating the helicity parameter of a chain-like cluster). More efficient algorithms (e.g. the disjoint set algorithm) should be implemented if clustering is required frequently during a simulation.

A.1.2 Gyration tensor

Given a cluster of particles with their Cartesian coordinates, the gyration tensor describes the geometrical distribution of the particles with respect to the cluster geometrical center. The gyration tensor is a 3-by-3 matrix of which each element is defined as:

$$S_{ij} = \frac{1}{N} \sum_{k=1}^N (r_i^{(k)} - r_c^{(k)})(r_j^{(k)} - r_c^{(k)}) \quad (\text{A.1})$$

where $i, j = 1, 2, 3$; N is the number of particles in the cluster; $\mathbf{r}^{(k)}$ and \mathbf{r}^C are the particle position and cluster geometrical center, respectively.

$$\mathbf{r}^C = \frac{1}{N} \sum_{k=1}^N \mathbf{r}^{(k)} \quad (\text{A.2})$$

The eigenvalues obtained from diagonalizing the gyration tensor reveal the overall shape of the cluster and the corresponding eigenvectors are the major axes. For example, if three eigenvalues are comparable, the cluster has a spherical shape; else if two comparable eigenvalues are much greater than the third, the cluster has a cylindrical shape. To quantify how spherical the cluster is, the asphericity parameter is then defined based on the eigenvalues of the gyration tensor:

$$A_S = \frac{1}{d-1} \sum_{i>j}^d (R_i^2 - R_j^2)^2 / \left(\sum_{i=1}^d R_i^2 \right)^2 \quad (\text{A.3})$$

where d is the dimensionality of the clusters, $d = 3$ in most cases; R_i^2 is the eigenvalues of the gyration tensor. The asphericity parameter varies from zero to unity, corresponds to a spherical shape and a cylindrical shape, respectively. If the cluster is close to spherical, it is common to use the radius of gyration R_g as an estimate of the radius of the sphere:

$$R_g^2 = \frac{1}{d} \sum_{i=1}^d R_i^2 \quad (\text{A.4})$$

A.1.3 Radial distribution function

The radial distribution function (RDF), or pair correlation function, $g_2(r)$, of a system gives the probability of observing two particles i and j separated by a distance r . The probability is usually normalized to the corresponding number density of an ideal gas at the same thermodynamic condition. Given the particles' position \mathbf{r}^N , the radial distribution function

at a separation r is defined as:

$$g(r) = \frac{1}{\rho} \sum_{i=1}^N \sum_{j=1}^N \delta(\|\mathbf{r}_i - \mathbf{r}_j\| - r) \quad (\text{A.5})$$

where $\rho = N/V$, N is the total number of particles of interest, V is the system volume, $\delta(\cdot)$ is the delta function, and $\|\cdot\|$ is the norm L2 operator giving the distance between two particles. Note that when periodic boundary conditions are applied, $g(r)$ is only meaningful when plotted for $r \leq L/2$, where L is the smallest box dimension. RDF provides the isotropic structural information of the system. For example, the distance corresponds to first peak indicates the nearest neighbor shell, to the second peak the next-nearest shell, and so forth. The RDF of a gas state does not have more than one small peak while that of a liquid state may have three distinct peaks. The RDF of a crystal exhibits numerous peaks separated by empty shells (Figure A.1).

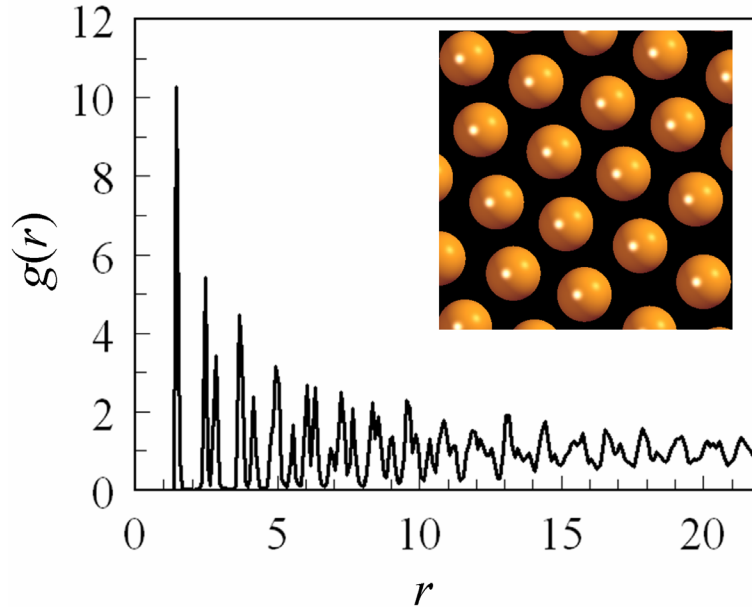


Figure A.1 Radial distribution function of a HCP lattice.

A.1.4 Bond order diagram

The bond order diagram (BOD) shows the local orientational ordering of a structure surrounding any given particle within some distance r or within a certain shell $[r_{min}; r_{max}]$. Since the local ordering in the first neighbor shell is often characteristic of the whole system, r is chosen to be the distance corresponding to the first peak in the radial distribution function.

Consider a system of N beads, for every particle, we loop through all of its neighbors, calculate the normalized displacement vector from the neighbor to the central particle and place this vector at some fixed origin. Figure A.2 shows an example of a BOD for the square grid structure formed by laterally tethered rods calculated from the center of mass of the rods within the shell of $[4.0\sigma; 5.0\sigma]$, corresponding to the spacing of the grid (see Section 6.1). The crowded regions indicate the relative position of the neighbors of each rod presumably placed at the center.

The bond order diagram is often used as a fingerprint for characterizing local structures and as an input for the Fourier shape descriptor in the shape matching library discussed below.

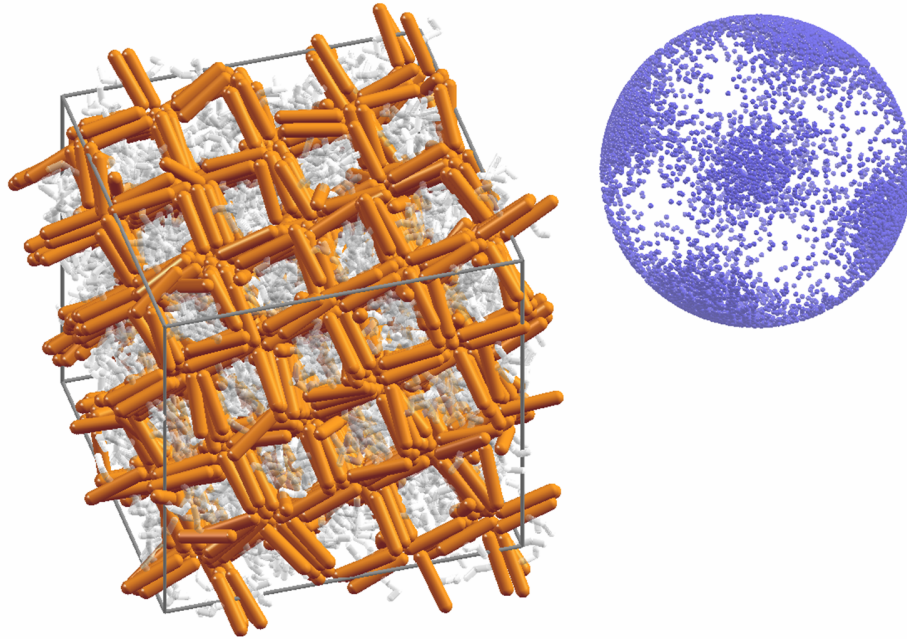


Figure A.2 Bond order diagram of a square grid structure.

A.1.5 Velocity autocorrelation function

The velocity autocorrelation function (VACF) is defined as:

$$C(\tau) = \frac{1}{N} \sum_{i=1}^N \frac{\langle \mathbf{v}_i(t_0 + \tau) \cdot \mathbf{v}_i(t_0) \rangle_{t_0}}{\langle \mathbf{v}_i(t_0) \cdot \mathbf{v}_i(t_0) \rangle_{t_0}} \quad (\text{A.6})$$

The VACF shows how fast a system in equilibrium relaxes, or equivalently, how the dynamics of the system becomes uncorrelated over time. The relaxation time of the system

can be approximated when $C(\tau)$ decays to zero. Note that τ is not the actual time step in a simulation but the lag between two samples taken at different time slices. To have a good statistical estimate of $C(\tau)$, the reference snapshots t_0 should be independent of each other. An example of the VACF of an equilibrated system is shown as Figure A.3.

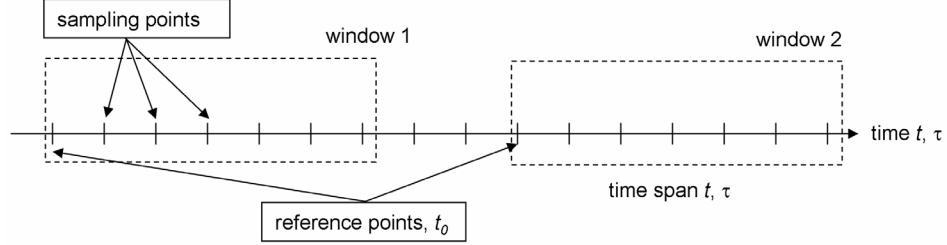


Figure A.3 Velocity autocorrelation function of an equilibrated Lennard-Jones system.

Assume that we have velocities dumped into 100 data files every 10000 steps, $v.t^*.dat$, for example, from $t = 39 \times 10^6$ to $t = 40 \times 10^6$. The time span for $C(\tau)$, or the maximum distance between two time slices, is half of this window, i.e. $\tau = 0 - 5 \times 10^5$. First, we should select the number of reference points N_{refs} used for the ensemble average. For example, $N_{\text{refs}} = 6$ equally spaced reference points at $t_0 = 390 \times 10^5$; 391×10^5 ; 392×10^5 ; 393×10^5 ; 394×10^5 and 395×10^5 . The bigger N_{refs} and the more distant between reference points, the better the statistics. Figure A.4 illustrate the reference points and sampling points used in this calculation.

Next, we choose the spaces between the time slices, τ , which can follow a linear or a logarithmic scale. For example, a linear scale gives $\tau = 0$; 10000 ; 20000 ;...; 5×10^5 ; meanwhile, a logarithmic scale $\tau = 0$; 10^4 ; 2×10^4 ; 5×10^4 ; 10^5 ; 2×10^5 ; and 5×10^5 . The minimum nonzero value of τ is the interval between two data files, and the maximum is the time span. This means, for example, with the linear scale above, we are using the velocities at $t = 39210000$; 3920000 ; 39230000 ;... to compute against the velocity at $t_0 = 392 \times 10^5$.

A.1.6 Mean squared displacement

The mean squared displacement (MSD) is defined as:

$$\langle r^2(\tau) \rangle = \frac{1}{N} \left\langle \sum_{i=1}^N \| \mathbf{r}_i(t_0 + \tau) - \mathbf{r}_i(t_0) \|^2 \right\rangle_{t_0} \quad (\text{A.7})$$

The MSD gives the mobility of the system at a given state point. It essentially is the average distance that a given particle travels after time τ . The slope of the MSD plotted ver-

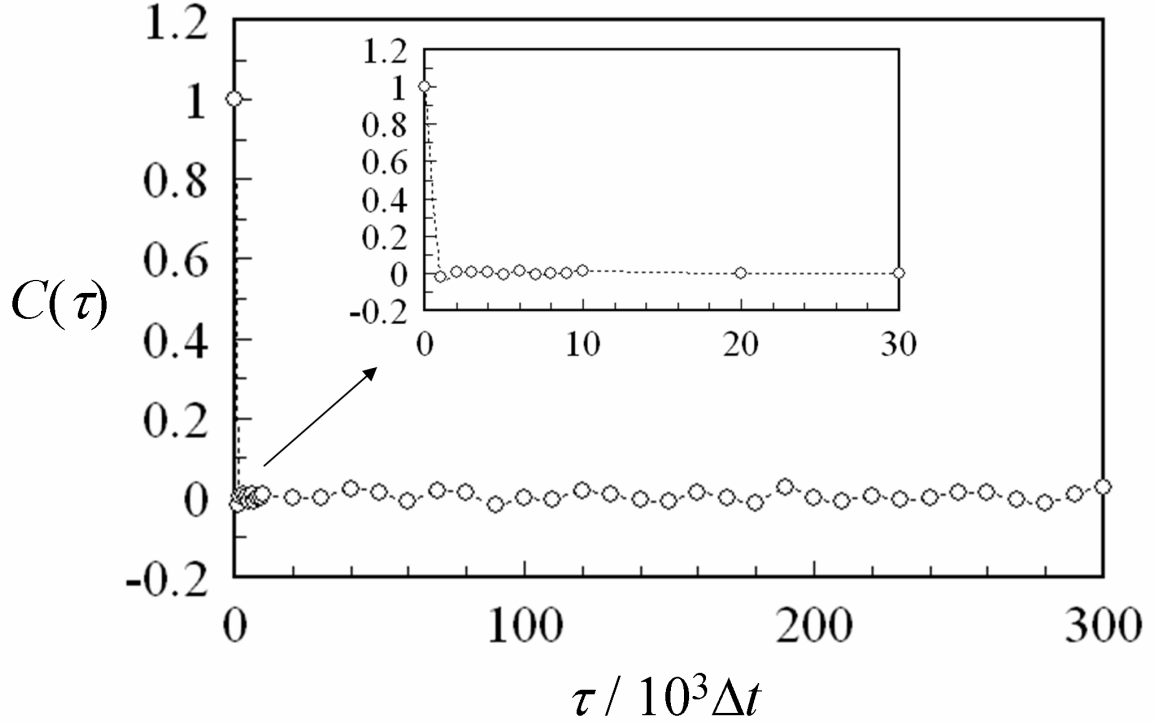


Figure A.4 Reference points and sampling points for calculating VACF.

time at large τ giving the self-diffusion coefficient, D , according to Einstein's equation: $\lim_{n \rightarrow \infty} \langle r^2(\tau) \rangle = 2dD\tau$ where d is the system dimensionality. An example of the MSD plot is shown in Figure A.5. At high temperature, the system is diffusive indicated by the positive slope of the MSD at large time intervals. As temperature is decreased, the particles start crystallizing and the slope of the MSD becomes zero at large time intervals.

The calculation of MSD is similar to that of VACF as described above, which involves comparing the particle positions at different states against a reference point, and averaging over several reference points. For example, we want to plot MSD for $\tau = 0 - 10^4$, with the interval of 200, meaning that there would be 50 points in the MSD plot. Assume that we have dumped out atom positions with images included into files at time steps: 11000100; 11000200; 11000300;... In order to compute the MSD at τ , we need to pick a number of snapshot pairs, calculate the distance between them, and average over the number of pairs. The number of pairs is sometimes called the number of windows, or the number of origins, or reference states. The average is performed over the number of windows. Say, for MSD($\tau = 500$), with 10 windows, we pick 50 snapshot pairs at (11000100; 11000600), (11000300; 11000800), (11000600; 11001100), etc. For each pair, we calculate square

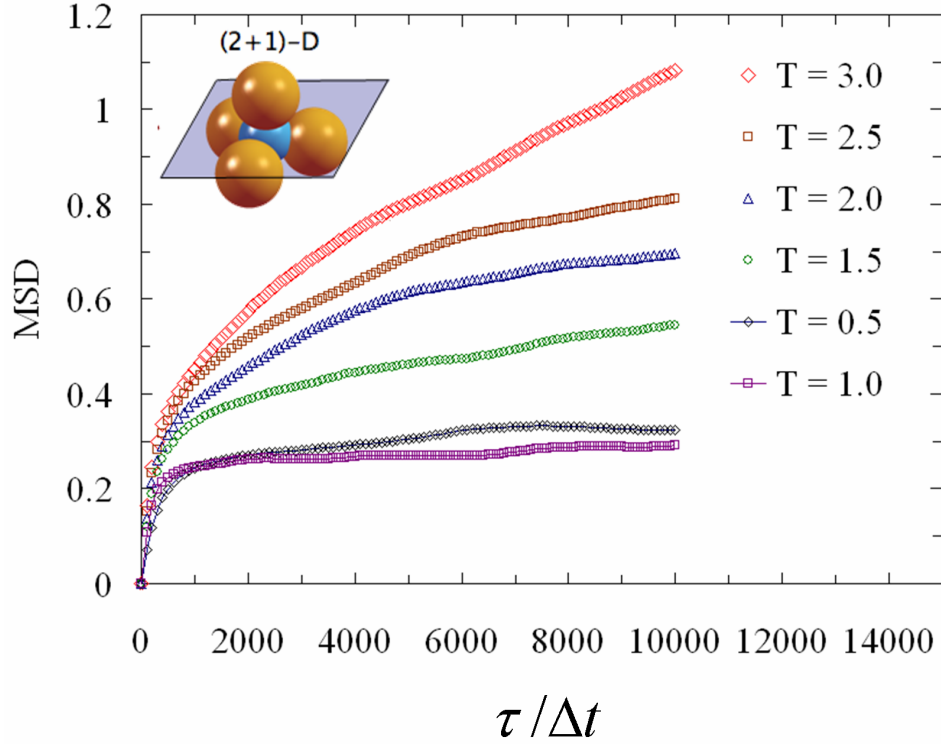


Figure A.5 Mean squared displacement of an equilibrated system of three-lock particles with the keys (blue) confined in a plane. See Section B.1.

displacement of individual particles and average over all the particles:

$$\frac{1}{N} \sum_{i=1}^N \|\mathbf{r}_i(t_0 + \tau) - \mathbf{r}_i(t_0)\| \quad (\text{A.8})$$

and then average the sum over the number of pairs. Note that we can change the distance between the origins, in this case, 300 to ensure that the reference points are uncorrelated for a good statistics; or choose τ for MSD from a logarithmic scale rather than a linear scale. Note that to exclude the translational motion of the whole structure from MSD, the center of mass of the system should be kept fixed; or the total momentum should be zero.

A.2 Shape matching order parameters

Shape matching order parameter is a generic order parameter that can be applied a wide range of structural characterization. The order parameter is a measure of the degree of the similarity between a sample structure to a reference one through a shape descriptor.

The shape descriptor is essentially an array of information that uniquely characterizes the reference structure, for example, the Cartesian coordinates of the atoms, the peak locations in the diffraction pattern, or the coefficients of the spherical harmonics expansion. Although bearing the term "shape matching", the order parameter can be extended to incorporate arbitrary aspects other than just geometry-related information. By definition, the difference between the shape descriptor of the sample structure and that of the reference structure, often transformed into a scalar value, gives the matching between these two structures. The difference is often normalized between zero and unity, corresponding to an uncorrelated and a perfect match, respectively. Further detailed explanation of the shape matching order parameter and its applications is given in Reference [221].

In this thesis, we use SMAC (Shape Matching Analysis Code), a open-source C++ library developed by Keys et al.[221], to calculate the shape matching order parameter based on a shape descriptor. The library is available for download in the Glotzilla package. Unlike conventional order parameters characterizing helicity, asphericity and chirality that requires particular mathematical formulation, the application of shape matching order parameters is more generic and flexible. The general procedure is as follows:

Choose a reference structure The reference structure can be either an ideal structure from other database or the final structure which has the desirable properties.

Plot the radial distribution function for the particles of interest for the reference structure The peaks in the RDF plot indicate the location of the shells in which most of the neighbors of a particle in the structure locate. Normally, the first peak is the most important because the interaction is short-ranged in our system and almost negligible to the next-nearest neighbor shell. Exceptions are hierarchically assembled structures formed by a bilayer sheet in Chapter 5.

Plot the bond order diagram at the vicinity of the shells Since the bond order diagram shows the orientational ordering of the neighbors relative to the central particle, we can choose the shells that are characteristic of the reference structure.

Use the location of the shells as input for the shape descriptor When the shells of interest are not spatially adjacent to each other, the particles in the intermediate shells can be disregarded. Multiple choices of the shape descriptor are available in SMAC.

Calculate the scalar metric of the shape descriptor of the reference structure and sample structures

Calculate the difference between the shape descriptors By default, a shape matching order parameter equal to unity corresponds to a perfect match. Since the most uncorrelated match can still have a nonzero matching value, the order parameter should be scaled between unity and the uncorrelated matching to show a good distinction between two extremes. Certainly, the choice of the most uncorrelated is up to the users.

The users need to write a C++ driver program to call these functions using the built-in data structures such as the Fourier shape descriptor, particle coordinates and simulation box data. To compile the program, the compiler (and linker) should be provided with the path to the header files and to the SMAC library. Documentation and examples can be obtained by contacting Glotzer group at <http://www.engin.umich.edu/dept/che/research/glotzer/>.

Appendix B

Preliminary simulations of reconfigurable and patchy particles

In this appendix, we present our preliminary results on lock-and-key colloidal particles and patchy particles. We show that the reconfigurability of the lock-and-key particles, represented by the mobility of the "lock" particles around the central "key" particle, plays an important role in stabilizing ordered structures other than triangular lattices. We also demonstrate that patchy particles with linear patches self-assemble into helices with a unique handedness. The geometry of the helices are shown to be dependent upon the arrangement of the patches and particle diameter. Though preliminary, our results serve as proof-of-concept for designing complex structures via novel building blocks with reconfigurability and with anisotropic interactions. Our future work would be to further characterize the thermodynamic stability of these structures and to have better statistics for the present results.

B.1 Lock-and-key colloidal particles

B.1.1 Introduction

Lock and key colloidal particles result from the depletion force between colloidal particles with and without dimples, namely, the locks and keys, respectively[3]. The lock-and-key binding results from the entropic gain of depletant molecules escaping from the dimples, causing an effective pulling on the keys towards the dimples. While the binding energy between the locks and the key is strong, in the order of $10k_B T$, the locks are able to rotate around the key, allowing for a unique reconfigurability within the building blocks, which is absent in rigid particles. Additionally, the overlapping between the locks and the key distinguish a system of these particles with that of a mixture of spheres with different sizes.

These features coupled with a plenty of parameters such as the number of locks per key, the center-center distance between the key and the locks, the lock and key size ratio, the confinement condition and the lock mobility relative to the key suggest that these colloidal building blocks are likely to give rise to novel assembled structures. Here we resort to computer simulations to investigate the assembled structures following the parameter axes in Figure B.1. We show that crystalline structures such as HCP or rhombic packing can form within some range of the size ratio and bond length. The constraint and stoichiometry between the locks and keys gives rise to the formation of degenerate crystalline structures of the keys. Also, the confinement in a quasi-3D space contributes to the formation of several unprecedented structures for four-lock particles. The simulation results serve to inspire further experimental study and fabrication of these interesting nanoscale building blocks. This work is conducted in collaboration with Pine’s group, and the results presented here should be considered a preliminary study as proof-of-principle.

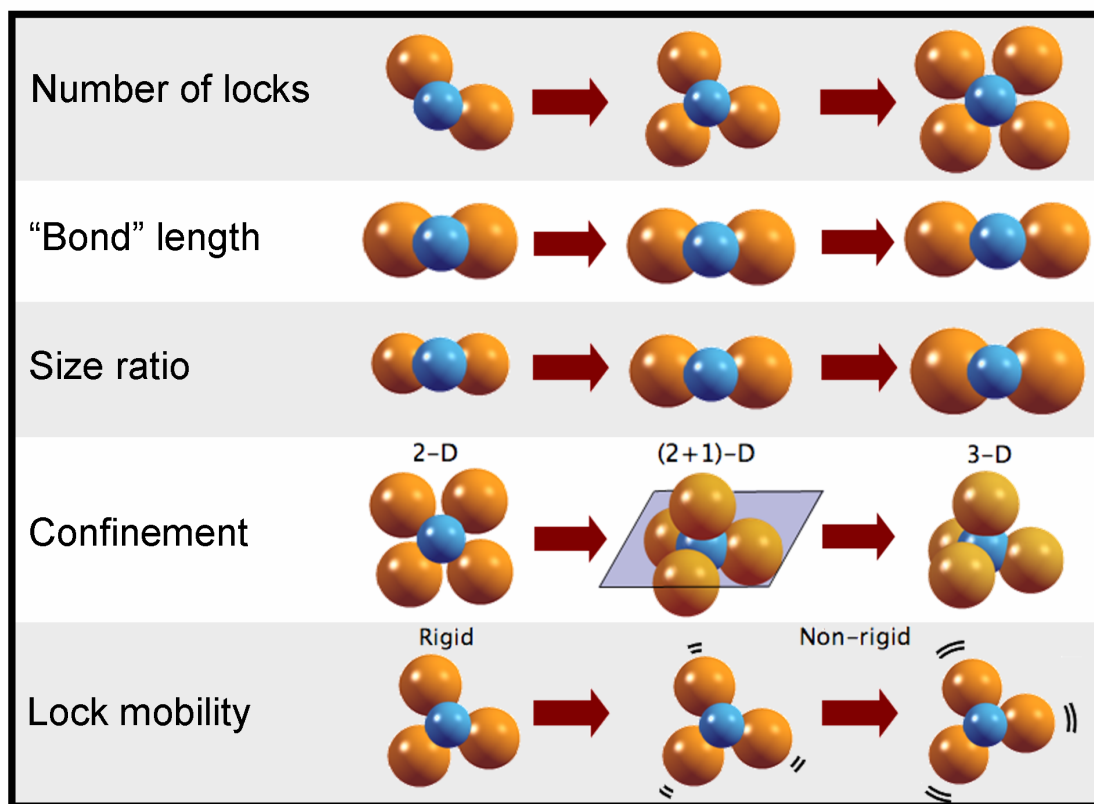


Figure B.1 Parameters that influence the self assembly of lock and key colloidal particles

B.1.2 Model and simulation method

Model

Colloidal particles are hundreds of nanometers in size. The key particles are spherical in shape, while the lock particles resemble a pac-man with a curved mouth. The keys and the locks do not directly interact with each other in a pure solvent. When tiny polymers are introduced into the solvent, these polymer molecules attempt to escape from the gap between close colloidal particles to gain more entropy, causing a pressure drop in the gap as compared to the pressure in the bulk. This pressure drop serves as a net "attractive force" pulling two colloidal particles close together. That "attractive force" is called the depletion force[51].

The depletion force induced when the key comes close to the mouth of the lock is much bigger than when the key comes close to any other (convex) part of the lock (partly because the polymers gain more entropy by escaping from the mouth), $10k_B T$ vs $1k_B T$. As a result, when the key fits into the mouth, the key and the lock are "permanently bonded" at the given temperature. The maximum number of locks per key is constrained by hard-sphere geometry, i.e. the lock/key size ratio and the mouth size. The locks are able to rotate around the key.

We consider several scenarios to model lock and key particles depending on the lock mobility and confinement considerations as follow:

Table B.1 Assembled structures formed with different rod lengths and the dimensionality of the periodicity of the structures.

2D particles	The locks are bonded to the key by stiff harmonic springs in the non-rigid model or the bond length is constrained by using the SHAKE algorithm in the rigid model.
2D rigid particles	Every particle is treated as a rigid body.
Quasi-3D particles	The locks are bonded to the key by stiff harmonic springs in the non-rigid model, or the whole particle is treated as a rigid body in the rigid model. However, the keys are constrained to move on a plane while the keys are allowed to rotate out of the plane.
3D particles	Non-rigid or rigid particles are allowed to move in 3-D space.

According to experiments, the size ratio between the key and the lock is approximately $D_K/D_L = 0.75$. We choose the key diameter to be $D_K = 1.0\sigma$, the lock diameter is the $D_L = D_K/0.75 = 1.33\sigma$. We also investigate different values of the size ratio in the range of 1.2-1.75. The distance between the lock and the key within a pacman d_{LK} is held by a stiff

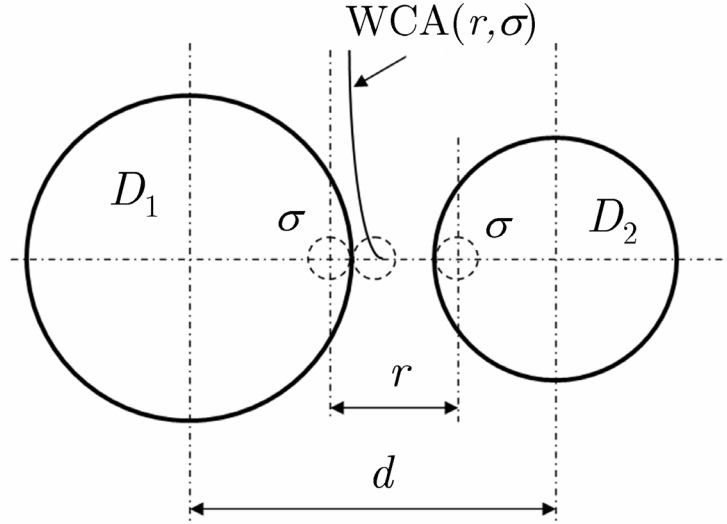
string with the spring constant of $k = 3000$. By choosing different spring natural lengths R_0 , we can adjust d_{LK} within some tolerance effectively similar to using SHAKE. However, at a sufficiently high density, or pressure, the springs can be compressed and the deviation in the bond length becomes greater as compared to using SHAKE.

The non-bonded interaction between the locks and keys are short-ranged as compared to their diameter. We use the Lennard-Jones 12-6 potential truncated and shifted to zero with different σ and δ as follow:

$$U_{LJ-shifted}(r) = \begin{cases} 4\epsilon \left[\left(\frac{\sigma}{r-\delta} \right)^{12} - \left(\frac{\sigma}{r-\delta} \right)^6 \right], & r \leq r_C + \delta \\ 0, & r > r_C + \delta \end{cases} \quad (\text{B.1})$$

where $\delta = (D_1 + D_2)/2 - \sigma$, D_1 and D_2 are the lock and key diameters, respectively.

We shift the potential towards the particle surface and use a value of σ_{LJ} much smaller than the particle diameter to capture the short range interaction between colloidal particles. For example, in Figure B.2 $\sigma_{LJ} = 0.1\sigma$, $D_1 = 1.0\sigma$ and $D_2 = 1.33\sigma$. At high pressure, the particles interact via the WCA potential with $r_C = 2^{1/6}\sigma_{LJ} = 0.1122\sigma$. At low density, the depletion attraction between the locks and keys is modeled by the LJ potential with $r_C = 2.5\sigma_{LJ} = 0.25\sigma$. The depletion attraction between the locks is in the order of $k_B T$.



$$r \leftarrow d - [(D_1 + D_2)/2 - \sigma] \equiv d - \delta$$

Figure B.2 Shifted 12-6 Lennard-Jones potential truncated at $r_C = 2^{1/6}\sigma_{LJ} = 0.1122\sigma$ to capture the short-ranged repulsion between particles.

Simulation method

We use Brownian dynamics to simulate systems of constant number of colloidal particles at constant temperature and volume, i.e. canonical ensemble. The systems are initialized at athermal conditions, i.e. all interactions are purely repulsive, for being well-mixed. For high pressure simulations, the box is gradually compressed or rescaled until crystallization is observed. To relieve defects, the box might be slightly expanded in a short time period, and then re-compressed. For low pressure simulations, the box is rescaled until the packing density reaches 0.3-0.4 to facilitate the aggregation of the particles.

B.1.3 Results and discussion

We focus on the parameters that are readily tunable in experiments in Pine's group at the time of this thesis being written. The parameters of interest are the lock-key distance (bond length), lock-key size ratio, lock mobility, number of locks per key, and spatial confinement as shown in Figure B.1. We investigate the assembly at high density and low density limits and show that the mobility of the locks plays a more influential role in the packing pattern of resulting structures at low pressure than at high pressure.

High density limit

Lock-key distance and size ratio Considering the two-lock particles, we investigate the size ratios $D_L/D_K = 1.2; 1.33; 1.5$ and 1.75 , which are in the range of the particles in practice. For each value of D_L/D_K , we vary the center-center distance between the lock and the key in the range of $(D_L/2; (D_L + D_K)/2)$. The lower bound corresponds to the case where two locks touch each other, and the upper bound to the case where the lock touch the key. $D_K = 1.0\sigma$ for all cases. The structures under comparison are obtained at a packing density of 0.85.

We observe that the locks (yellow) can form a hexagonal close packing (HCP) structure for a certain range of d_{LK} and r . Representative snapshots in Figure B.4 compare a good HCP structure (Figure B.3(a)) versus a disordered structure (Figure B.3(b)) of the locks at $D_L/D_K = 1.33$. The peaks in the diffraction pattern (Figure B.4(a), middle) are indicative of the six fold symmetry of the HCP structure of the locks. The keys (blue) are located on a degenerate kagome lattice due to the constraint: every key has two and only two locks. The diffraction pattern of the keys (Figure B.3(a), bottom) shows the peaks corresponding to the underlying HCP lattice formed by the locks. The noisy parts surrounding the peaks

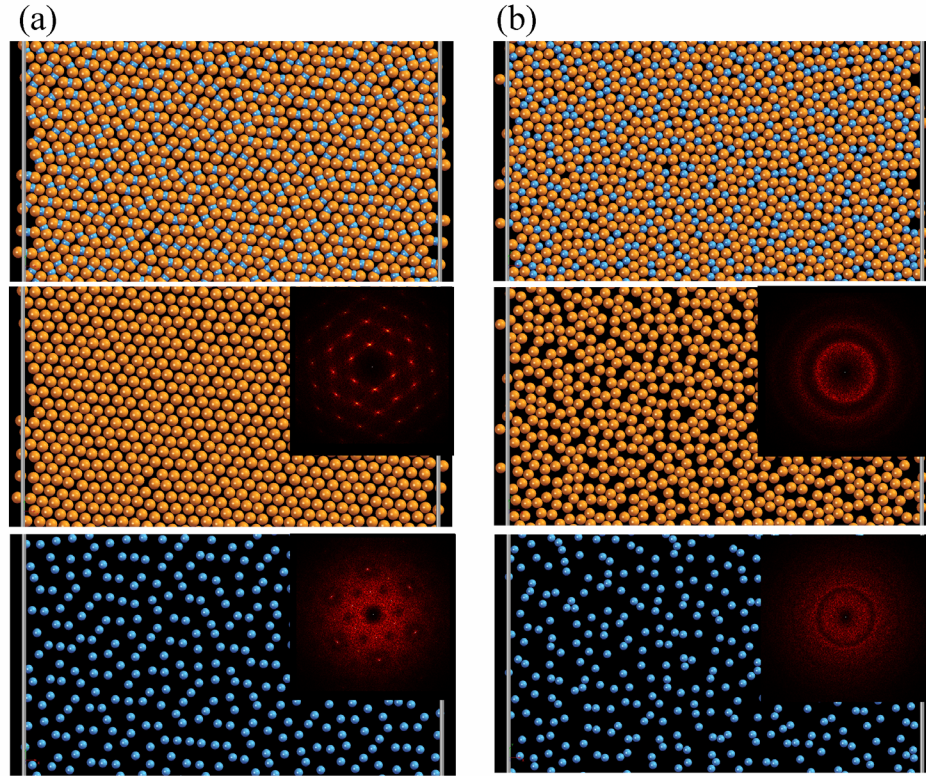


Figure B.3 Structures formed by 2-lock particles with (a) $d_{LK} = 0.75\sigma$ and (b) $d_{LK} = 1.0\sigma$ for the size ratio $D_L/D_K = 1.33$. Top: snapshot with the keys in blue and locks in yellow. Middle: only the locks are visualized. Bottom: only the keys are visualized. Insets are the diffraction patterns.

correspond to the disordered arrangement of the keys. On the contrary, for the disordered structure neither the diffraction pattern of the locks or that of the keys shows any peak (Figure B.3(b)).

The distribution of the bond angle shown in Figure B.4 demonstrates the conformation of individual particles ($D_L/D_K = 1.33$) within the final structures. In a HCP structure ($d_{LK} = 0.7\sigma$), the two-lock particles adopt a uniform linear geometry with most of the angles being 180° . As the bond length increases ($d_{LK} = 0.9\sigma$ and 1.1σ) the distribution is shifted towards smaller angles and becomes more polydisperse, corresponding to more disordered structures. For $d_{LK} = 1.1\sigma$, where the depth of the locks is the most shallow, the peak around $\theta = 76^\circ$ indicates that $\approx 20\%$ of the particles have adopted a V shape with two locks touching each other, which makes them incompatible with the packing into a HCP structure.

Lock mobility The mobility of the locks of a particle can be characterized by the free volume accessible by the locks on the key surface. For a given size ratio D_L/D_K the greater

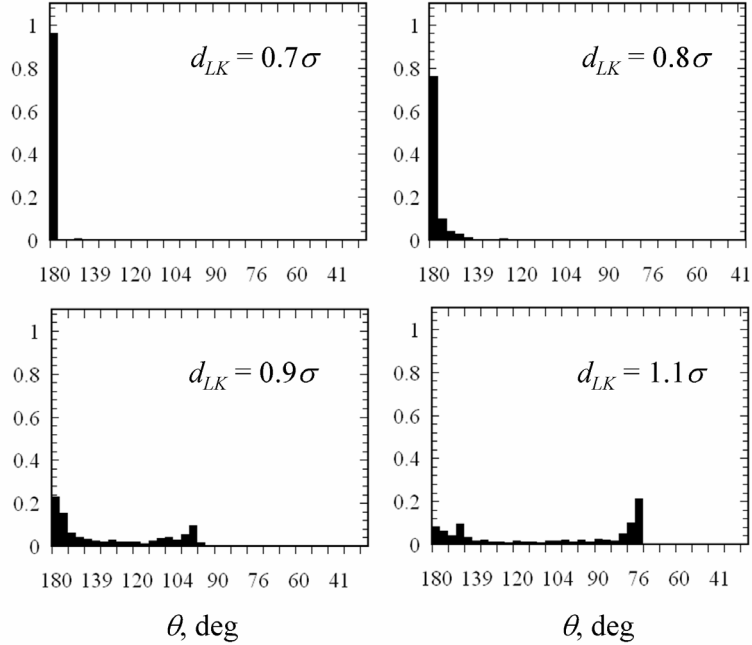


Figure B.4 Distributions of the bond angle of individual two-lock 2D particles ($D_L/D_K = 1.33$) with different bond lengths.

the distance d_{LK} , the greater the lock mobility because the locks have more accessible volume on the key surface. We choose the best HCP structure of the locks for a given value of D_L/D_K as the reference state and calculate the shape matching order parameter of the final structures obtained for each pair of $(D_L/D_K, d_{LK})$. As can be seen in Figure B.5(a), the optimal range to observe the HCP structure is shifted to higher values of d_{LK} as the size ratio increases. That range of d_{LK} is equivalent to the optimal range of the lock mobility for the stabilization of the HCP structures at a given size ratio. Beyond that range of the lock mobility the particles form a disordered solid.

Another approach to completely remove the lock mobility is to make the particles rigid by fixing the relative position of the locks with respect to the key. We infer from Figure B.4 that in a HCP structure, the particles are most likely to have a linear shape; thus, we consider the case where the locks and key are “frozen” in a linear geometry, making a dumbbell-shaped rigid particle. Figure B.5(b) shows the HCP order parameter for rigid particles as a function of D_L/D_K and d_{LK} . Comparing the HCP order parameter in Figure B.5(b) with that in Figure B.5(a), we observe a similar behavior, i.e. there is an optimal range of d_{LK} for each value of size ratio D_L/D_K in which the locks form an ordered HCP structure. The range is also broadened to higher values of d_{LK} for a given value of D_L/D_K . For example, for $D_L/D_K = 1.33$, the rigid particles assemble into a HCP structure as d_{LK} does not exceed 0.95σ ; meanwhile, the lock mobile particles can retain the HCP structure

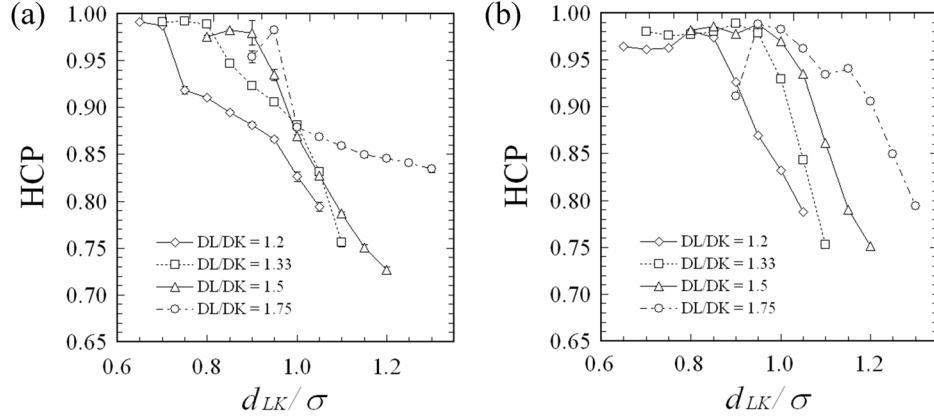


Figure B.5 HCP shape matching order parameter with different lock-key size ratio (D_L/D_K) and bond length d_{LK} . Each curve is obtained by averaging across several independent runs. Error bars are smaller than the marker size. (a) Locks are able to move around the key. (b) Locks and key within a particle are rigid into a linear geometry.

up to $d_{LK} = 0.8\sigma$.

Number of locks per key In addition to two-lock particles, we consider particles with three and four locks, also varying the bond length and size ratio. Similar to two-lock particles, the locks of these particles can form crystalline structures within an optimal range of lock-key bond length and size ratio. Beyond the optimal range the assembled structure do not exhibit any long range order. In their crystalline states, the locks of three- and four-lock particles assemble into a HCP lattice and a rhombic lattice, respectively.

For three-lock particles the bright peaks in the diffraction pattern of the keys in the crystalline state indicates that the keys are constrained within the HCP lattice of the locks (Figure B.6(a)). The noise surrounding the peaks shows their local disorder. The dark lines correspond to the space occupied by the locks that is inaccessible to the keys.

The keys of four-lock particles are restricted in a rhombic lattice of the locks as indicated by the peaks in the diffraction pattern (Figure B.6(b)). The snapshot shows the presence of several grain boundaries caused by the finite relaxation time in our simulations. The orientation of the grains is shown in the bright stripes in the diffraction pattern. We note that unlike for two- and three-lock particles, the locks of four-lock particles compromise between forming a rhombic lattice and forming a triangular lattice. The former results from intra-particle constraints, i.e. the square shape of the particles; the latter results from inter-particle constraints, i.e. the locks from neighboring particles always tend to pack into a HCP lattice.

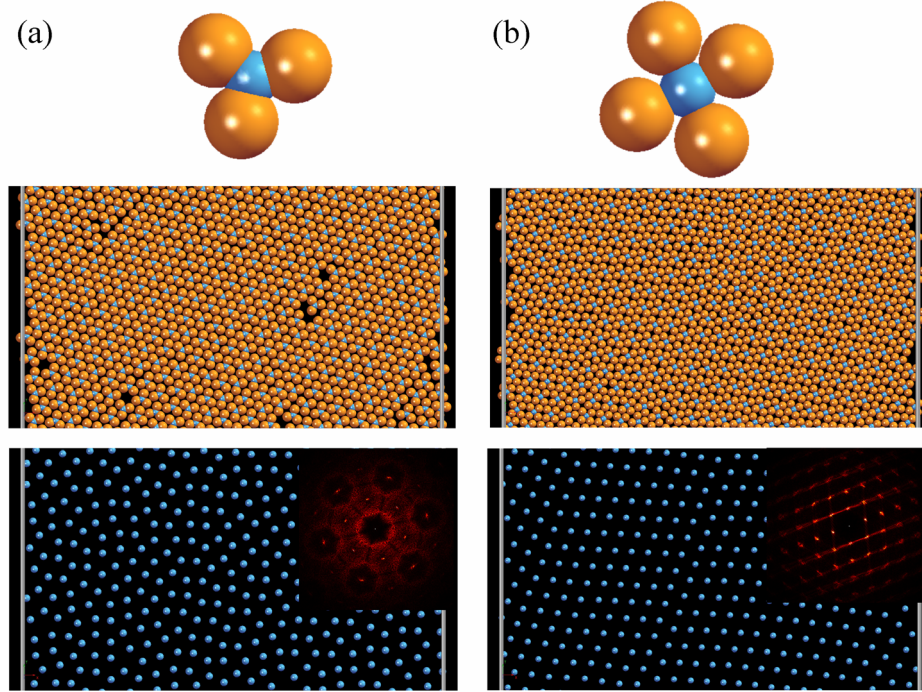


Figure B.6 Crystalline structures formed by (a) three-lock ($d_{LK} = 0.75\sigma$) and four-lock ($d_{LK} = 1.0\sigma$) particles for $D_L/D_K = 1.33$. The bottom images show the keys only with the diffraction pattern.

Spatial confinement We extend the spatial confinement from 2-D to quasi-3D, where the keys are confined in the x-y plane and the locks are able to rotate out-of-the plane. This confinement is to reproduce the experimental condition where the particles can move within a thin film or on a substrate without diffusing to the z direction. We choose to show the results of the three-lock particles; the simulations for two- and four-lock particles are underway. We vary the bond length and size ratio and observe the formation of different packing patterns at the packing density of 0.7.

As can be seen in Figure B.7, there is a disordered-ordered transition in the assembled structure of the locks as the bond length decreases. For $D_L/D_K = 1.33$ the transition occurs between $d_{LK} = 0.95\sigma$ and $d_{LK} = 1.0\sigma$. For smaller bond lengths, the crystalline structures exhibit a four-fold symmetry at $d_{LK} = 0.95$ and $d_{LK} = 0.9\sigma$.

We compare the crystalline structures formed at $d_{LK} = 0.8\sigma$ and $d_{LK} = 0.9\sigma$ in Figure B.8. As indicated by the bond order diagram measure for individual particles, the particles adopt a tri-star shape for $d_{LK} = 0.8\sigma$ (Figure B.8(a)) and a T shape for $d_{LK} = 0.9\sigma$ (Figure B.8(b)). The difference in the particle conformation leads to different packing patterns as shown in Figure B.7. The star shape particles tilt with respect to the x-y plane and stack into rows to have an efficient packing.

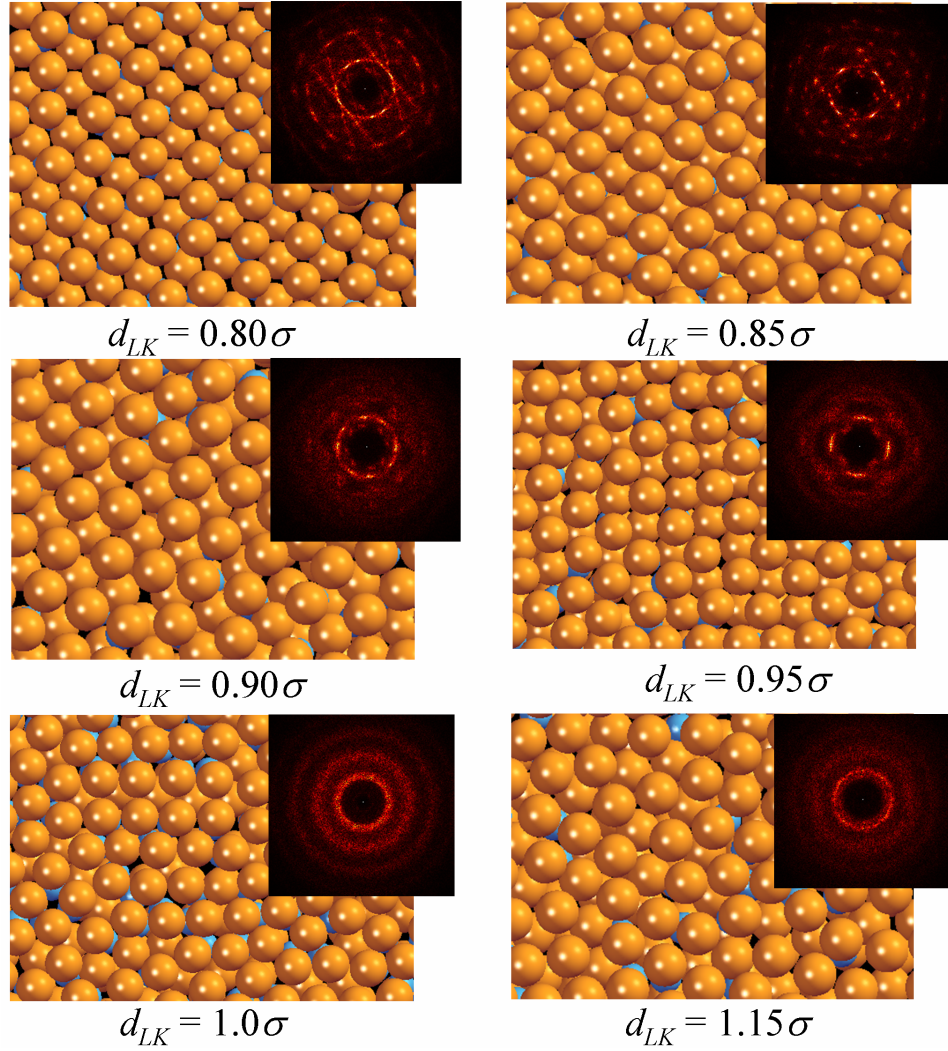


Figure B.7 Assembled structures formed by three-lock particles with the keys constrained on the x-y plane with different bond lengths for the size ratio of $D_L/D_K = 1.33$.

B.1.4 Low density limit

We investigate the self-assembly of two- and three- lock particles in 2-D space at the low density ($\phi < 0.1$). The motivation for studying this limit is to phase out the effects of high pressure on the lock mobility. The aggregation of the particles is induced at $T^* = 0.25$ in a simulation space sufficiently large to avoid periodic boundary effects. We found that the size ratio, bond length and lock mobility altogether give rise to unique tiling patterns that are not observed for rigid particles.

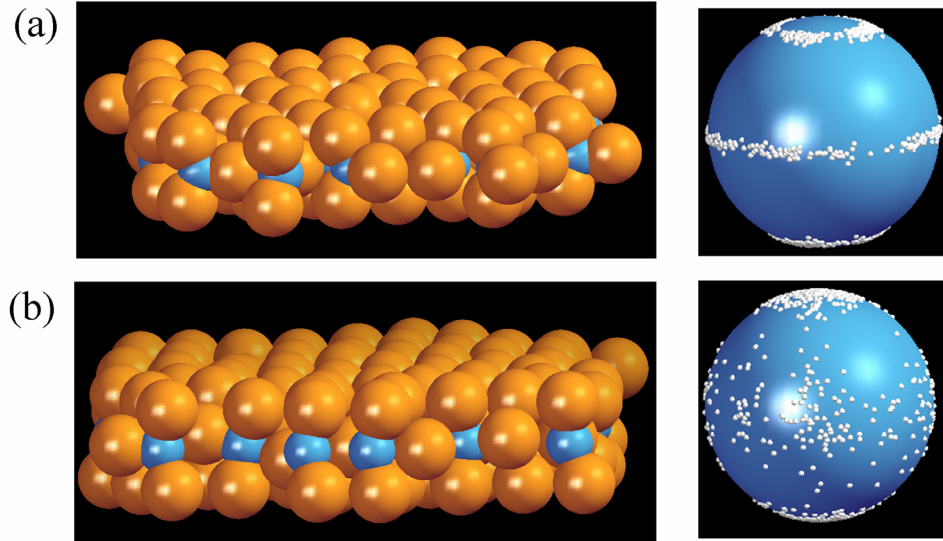


Figure B.8 Four-fold symmetry structure formed by quasi-3D three-lock particles. (a) $d_{LK} = 0.8\sigma$; $D_L/D_K = 1.33$ and (b) $d_{LK} = 0.9\sigma$; $D_L/D_K = 1.33$. Left: Side-view of a portion of the assembled structure. Right: Bond order diagram of individual particles.

Two-lock particles

As shown in Figure B.9, the locks of two-lock particles form a HCP lattice for $D_L/D_K = 1.75$ or an aperiodic lattice composed of triangles and squares for $D_L/D_K = 1.5$. For $D_L/D_K = 1.75$ and $d_{LK} = 0.9\sigma$ (Figure B.9, left), the locks form a hexagonal lattice at high density similar to that observed at high density (Figure A2.3(a)). The particles also adopt a linear geometry. In this case, the lock mobility is small and the HCP lattice is always favored regardless of density.

As the size ratio is decreased to $D_L/D_K = 1.5$ (Figure B.9, right), the lock mobility is increased, the HCP lattice does not form at low density as observed at high density (Figure B.5(a)). Instead, we found that the locks form a lattice composed of regular triangles and squares. The tiling pattern is a random mixture of the elongated triangular tiling ($3^2.4^2$) and snub square tiling ($3^2.4.3.4$). The Bragg peaks in the diffraction pattern of the locks suggests that there is an underlying 12-fold symmetry lattice in the structure. The bond angle distribution further reveals that the particles adopt a 120-degree conformation within the lattice. This is interesting because a small change in the size ratio, hence the lock mobility, could lead to a remarkable change in the packing pattern of the assembled structure.

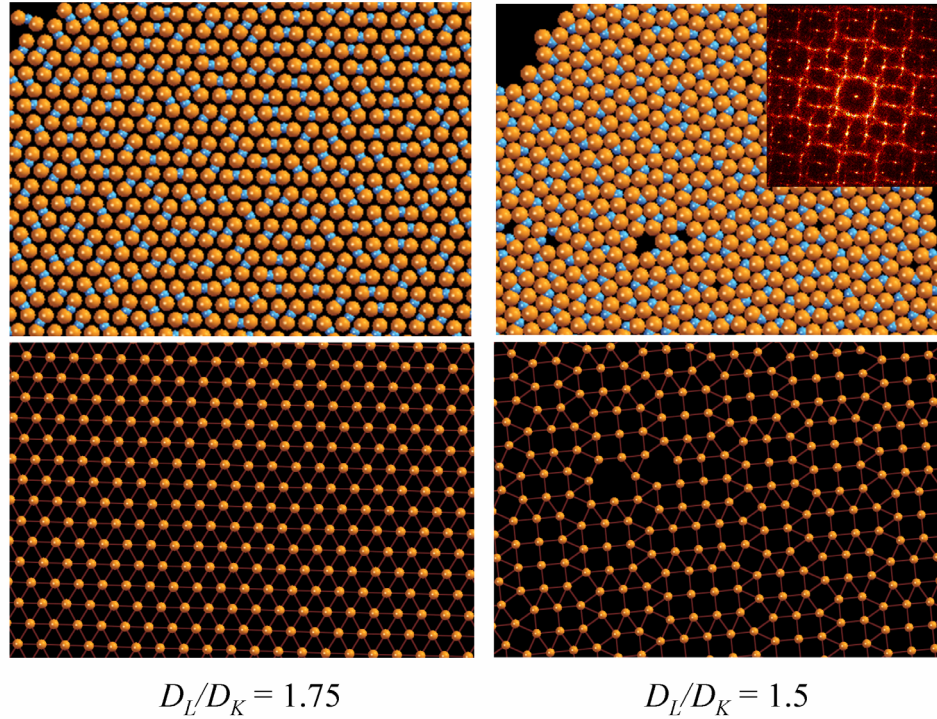


Figure B.9 Two-lock particles with the bond length of $d_{LK} = 0.9\sigma$ and different values of bond length D_L/D_K

Three-lock particles

Figure B.10 shows different assembled structures from three-lock particles with the same size ratio. As the bond length increases, the locks have more mobility on the key surface. For small lock mobility ($d_{LK} = 0.85\sigma$), the locks form a HCP pattern as expected because the particles all have a tri-star conformation. For higher lock mobility ($d_{LK} = 1.0\sigma$), the locks form an ordered lattice of oval-shaped tiles. The oval-shaped tiles are made of the particles in a T-shaped conformation packing side-by-side.

For a greater lock mobility ($d_{LK} = 1.15\sigma$), the locks form an aperiodic ordered lattice composed of triangles, rhombs and pentagons while the keys located at the center of the pentagons, aligning into stripes. The pentagons are coupled into pairs, surrounded by three rhombs and three triangles. The diffraction pattern of the locks indicates a long range ordering despite a non-trivial real-space pattern. Interestingly, within the lattice, the particles adopt a symmetric Y-shaped conformation with two locks touching each other and the third lying on the particle symmetric axis. Again, these results demonstrate that the lock mobility allows for the particles to assemble into structures much more interesting than HCP lattices.

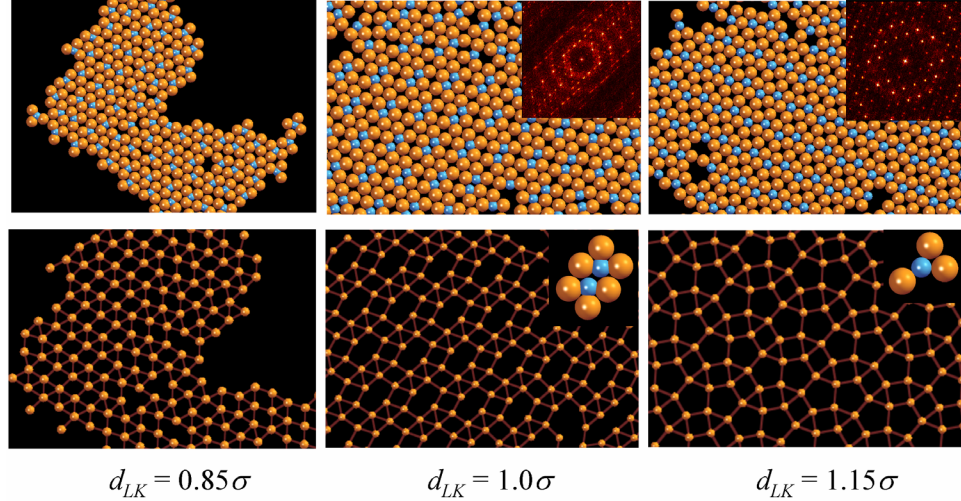


Figure B.10 Three-lock particles with a size ratio of $D_L/D_K = 1.33$ and different values of bond length d_{LK} . The lock mobility increases along with the bond length (from left to right)

B.1.5 Conclusion and ongoing work

We have investigated several parameters that strongly influence the self-assembly of lock-and-key particles. The most salient feature of these particles as compared to other previously studied building blocks is the lock mobility, which lends them a unique flexibility to have efficient packing. At high density, the size ratio and bond length play much more significant role than the lock mobility in stabilizing crystalline structures at high pressure or density. However, at low density, the lock mobility becomes more pronounced, allowing the particles adopt conformations that maximize the local packing fraction. As a result, the particles assemble into various structures with tiling patterns that are inaccessible with rigid particles with the same size ratio and bond length. Simulations on the described systems are underway for better statistics. Additionally, further characterization of the aperiodic assembled structures formed by three-lock particles at low density will be the focus of our future study.

B.2 Patchy particles

We aim at engineering helical structures from the self-assembly of spherical patchy particles with two linear patches, intentionally arranged to create a directional lock-and-key interaction between particles. This section presents preliminary results in this direction. Using molecular dynamics, we find that there is an optimal range of the particle size and patch arrangement that maximize the probability of such anisotropic building blocks assembling into helices. Within the optimal range, the assembled helices are shown to match with the

target structure as prescribed by geometry calculations and to be robust with the patch size. Out of this range, the building blocks are likely to aggregate into rings or random coils. The aggregation of the patchy particles can be characterized as an equilibrium polymerization as the monotonous growth of the cluster size and the continuous change in the system potential energy.

B.2.1 Introduction

The fabrication of next-generation functional materials has been favorable with the availability of assembling building blocks with diverse shape, size and chemical functionality. The anisotropy of assembling building blocks in fact can be characterized by a multi-dimensional parameter space as proposed by Glotzer et al.[25] including aspect ratio, patchiness, surface quantization, branching and roughness. Along one of these dimensions, the variation in the particle patchiness, or surface coverage, gives rise to a novel class of assembling building blocks, which are distinguished by their ability to robustly self-assemble into desired structures with high monodispersity. It is the highly anisotropic, strongly directional interactions between patches that allow the modified particles to interact in the same fashion as virus capsid proteins and many biological molecules. With the rapid progress in synthesis techniques since 1990s such as templating[155, 243], colloidal assembly[244, 245] or particle lithography[246], it is now possible to synthesize such patchy particles with multiple levels of complexity in a large batch volume. Theoretical models for patchy particles serving as a predictive tool for experiments have also been constantly developed in attempts to understanding the roles of anisotropic interactions, thermodynamic parameters and patch properties on the particle assembly behaviors. Examples for such theoretical models include the water-mimicking particles[247, 248], stick hard spheres[235, 249, 250], bumpy particles with distinguishable atoms[27, 251–254], particles with protein-like interactions[28, 29, 233, 255–260] and density functional theory models[261, 262]. Further details on fabrication methods can be found in a thorough review performed by Pawar et al.[263]

It has been shown that the self-assembly of patchy particles and their biological analogs such as virus capsid proteins and surface functional globular proteins depend on a large number of parameters in addition to thermodynamic variables and solvent conditions. The particle shape and the patch arrangement, geometry and selectivity are all identified as important factors that can influence the self-assembly significantly. Using molecular dynamics, Rapaport first showed how patchy particles in a trapezoidal shape easily assemble into capsid-like structures given that the interactions between the sticky spots follow certain rules

in sequence[251]. Relaxing those nonphysical rules, Nguyen et al. developed two other shape model patchy particles, both of which spontaneously assemble into capsid structures with different triangulation numbers[253]. In their work the special particle shape and the patch selectivity are key to the successful formation of capsid-like structures. The patch size and shape are also been shown to have profound effects on the formation of target structures. Wilber et al. studied the assembly of a five-patch particle with protein-like interactions, showing that the optimal patch width for icosahedral clusters results from the competition between energetic and kinetic requirements[29]. In 2004, Zhang and Glotzer proposed a bumpy particle model made of distinguishable "atoms", which allows for capturing the directional interactions between particles with a remarkable flexibility by specifying interactions between patch "atoms"[27]. They predicted a wide spectrum of assembled structures by varying the particle shape, patch arrangement, composition and geometry. For example, spherical particles form sheets when the patches are attached around the equator; triangular plates stack into a twisted structure with a linear patch on a face, and stair-case structures with V-shaped patches on two faces. If each linear patch is made of two dislike molecular types, the patches help align binding particles in an energetically favorable configuration. Later, they proposed a stick hard sphere model which assembles into diamond structures, which can be further stabilized by additional "bond" angle interactions. These inspiring results suggested that linear patches can be judiciously arranged to induce angle constraints on the aggregation of patchy particles. In this contribution, we extend the Zhang and Glotzer's model and introduce another family of assembled morphologies from patchy particles, helical structures with a uniform chirality. We show that the patchy particles successfully assemble into target helices dictated by the particle size and patch arrangement. By tuning the particle size and patch arrangement, we can drive the assembly of patchy particles from helices to linear chains and closed rings. We also find that the formation of the helices is robust over a considerable range of the patch width, suggesting that the patchy particles are likely to adopt a high propensity to form helices in experiments. The autonomous and precise formation of such helical structures serves to inspire the fabrication of functional nanostructures with unique electronic and optical properties, and more generally, to propose an approach to incorporate directional lock-and-key interactions into isotropic building blocks.

B.2.2 Model and simulation method

Model

We employed a generic coarse-grained model similar to the distinguishable atom model used by Zhang and Glotzer[27]. The patchy particles are treated as rigid bodies that are able to freely move in a three dimensional space. Each spherical patchy particle consists of N_S beads with diameter σ on the surface and two linear patches, each of which is composed of $N_F = 6$ beads, with the same diameter σ , of two molecular types. The arrangement of the linear patches is given by two angles ϕ and θ , determined by the particle center and the patch centers in the body-fixed frame. The patch width W and the patch height δ are defined as illustrated in Figure B.11. Because of symmetry, we show the results for θ in the range of $[0^\circ; 90^\circ]$ and ϕ in the range of $[0^\circ; 180^\circ]$. The assembled structures with the other ranges of these angles are identical but with the opposite handedness.

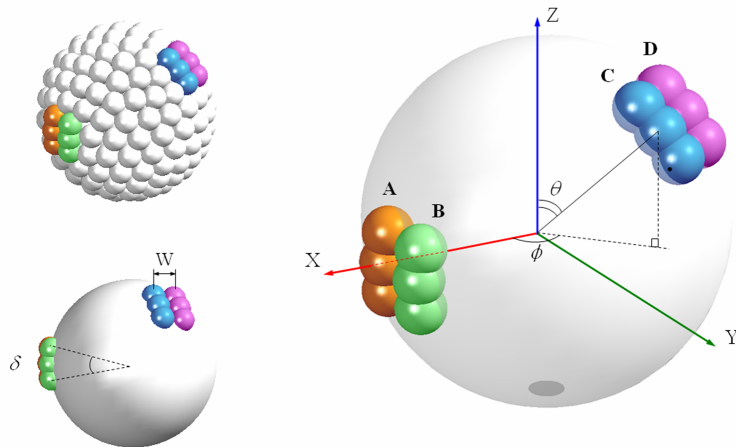


Figure B.11 Model patchy particle with two linear patches, each consisting of two non-attractive types of molecules (A, B) and (C, D). The top left figure shows the model for $D = 7.0\sigma$. The surface beads (white) are hidden in the bottom left and right images for clarity.

The interactions between the molecules in the patches are specified such that the patchy particles are energetically favored to aggregate into ring structures as indicated in Reference [27]. The obvious advantage of our model is that the anisotropic interaction between patchy particles is inherently incorporated in the linear shape of the attractive patches. As a result, isotropic interactions such as the standard Lennard Jones and Weeks-Chandler-Andersen potentials can be used to represent the attractive or purely repulsive interactions between constituent beads, respectively. Additionally, the coarse graining into bumpy spheres on the surface represents the interactions between actual patchy particles, which is short ranged as compared to the particle diameter. Specifically, the aggregation of the beads from attractive

stripes, i.e. (A; D) and (B; C), is modeled by the 12-6 Lennard-Jones potential truncated and shifted to zero at the cutoff distance of 2.5σ . The interaction between the non-attractive beads (the other pairs) is modeled by the Weeks-Chandler-Andersen potential.

Simulation method

Molecular dynamics is used to simulate a system of the model patchy particles in a three dimensional volume. We use the Nose-Hoover thermostat coupled with both the translational and rotational degrees of freedom of the rigid bodies such that our simulations sample the isothermal ensemble. The motion of the rigid particles, which are initialized randomly in the simulation box is achieved using the velocity Verlet algorithm with quaternions with a time step $\Delta t = 0.002\tau$. The number of particles (N_P) ranges from 64 to 216 to ascertain that the obtained structures are consistent. For each parameter set, we perform 4-5 independent simulation runs to ascertain that the results are consistent and statistically meaningful. The simulation results were produced using LAMMPS and HOOMD-blue, open-source parallel molecular dynamics codes.

B.2.3 Results and discussion

We first determine the temperature T^* below which the particle aggregation occurs. By monitoring the maximum cluster size and system potential energy at different temperatures, we find that the patchy particles assemble into clusters in analogy with equilibrium polymerization rather than a first-order phase transition. We then present the phase behavior of patchy particles with different particle sizes as function of the patch arrangement (ϕ and θ) at a sufficiently low temperature. Within the optimal range of ϕ and θ , the helix radius and pitch match perfectly with geometrical calculations, indicating that the self-assembly into target helices is well controlled. Additionally, the helices are shown to be robust with respect to a wide range of the patch size.

Assembly dynamics

We investigate the dynamics of the self-assembly of patchy particles with different values of (D/W , ϕ , θ). Our results reveal that the aggregation of patchy particles mainly depends on the reduced temperature T^* , i.e. the attraction strength ε between the patches and temperature T regardless of the particle size and patch arrangement. The system potential energy U at instantaneous temperatures and upon heating and cooling are shown in Figure B.12(a).

There is neither hysteresis nor discontinuity in U upon heating and cooling, indicating that the aggregation is analogous to equilibrium polymerization, rather than a first-order phase transition. To investigate the assembly dynamics, we start with a small size system of $N_P = 24$ patchy particles with $D/W = 5.0$, $\phi = 30^\circ$ and $\theta = 45^\circ$. The time evolution of the maximum cluster size at different temperatures for that system is shown in Figure B.12(b). For $T^* \geq 0.67$, the particles remain isolated and diffuse throughout the box, as indicated by the maximum cluster size being fluctuating around one and the system potential energy close to zero. The particles aggregate into robust clusters when the attraction strength between patches T^* is less than 0.67. The maximum cluster size increases versus time in a step-wise manner, suggesting that the particles first assemble into small aggregates, which subsequently merge into bigger clusters. The maximum cluster size reaches the total number of particles, indicating that the particles tend to form one big cluster. For a system of 1000 particles at $T^* = 0.25$, the average cluster size increasing (Figure B.12(c)) and the cluster size distribution shifting towards large values over time (Figure 2(d)) indicate that the particle aggregation is not size limiting. Patchy particles with other values of (D/W , ϕ , θ) also exhibit similar dynamic behaviors.

Energy landscapes

We investigate the effects of the patch arrangement and particle size while fixing the patch size ($W = 1.0\sigma$ and $\delta = 20^\circ$) on the assembled structures. Since the potential energy minimizing configurations are those in which the patches perfectly match each other, corresponding to helical structures for $\theta < 90^\circ$, the emergence of rings and random coils is considered competing morphologies with higher potential energy. The difference in the potential energy between the helices and their competing morphologies, however, becomes negligible when the chain gets longer. As a result, it is more likely to observe rings and coils than helices in certain ranges of (ϕ , θ). In the following, we show the energy landscape in terms of (ϕ , θ) where the structures reported in each color coded region have a frequency of occurrence greater than 60%. In general, the plots show the helical state is surrounded by higher energy barriers marked by rings and coils.

The energy landscape for the particle sizes of $D/W = 4.0, 5.0, 6.0, 7.0$ and 8.0 are obtained at $T^* = 0.25$. For $D/W = 4.0$, in addition to helices, spherical patchy particles may assemble into random coils and rings as by products (Figure B.13). At small ϕ and large θ , the patch centers are close to each other and to the particle equator; the particles tend to lock into rings similar to those in Reference [27] (Figure B.13(b)). For larger values of ϕ , the patches are more separated; and the particles are more likely to aggregate into random

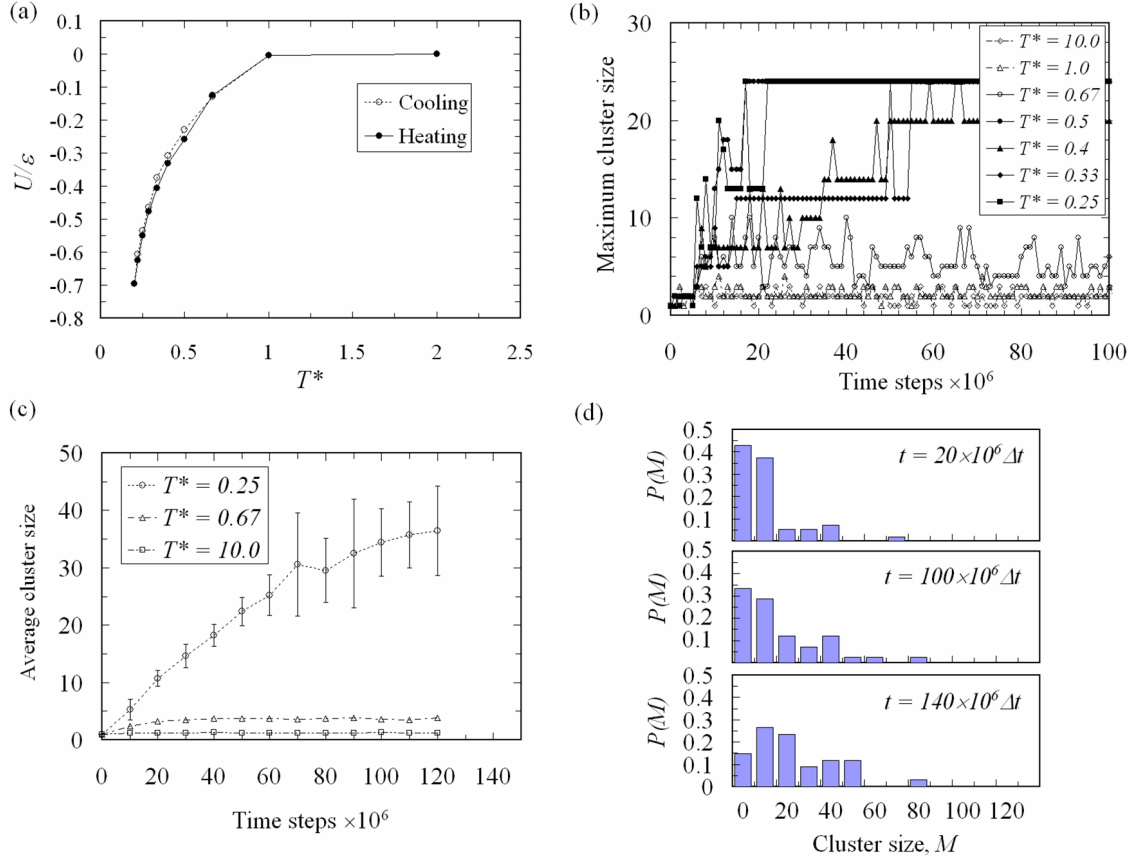


Figure B.12 Assembly dynamics: (a) Per particle system potential energy upon heating and cooling. Error bars are smaller than the markers. (b) Time evolution of the maximum cluster size versus time at different temperatures for a system of 24 particles. (c) Time evolution of the average cluster size for a system of 1000 particles at $T^* = 0.25$; 0.67 and 10.0. (d) The cluster size distribution for a system of 1000 particles at $T^* = 0.25$ as the system evolves.

coils (Figure B.15(c)). For small values of θ , the patch centers though close to each other are far from the particle equator, resulting the formation of helices (Figure B.13(d)). The comparable helix and coil regions suggest that there would be a competition between these two structures for patchy particles with $D/W = 4.0$.

For $D/W > 4.0$, the landscapes are divided into two regions: rings for $\theta = [60^\circ; 90^\circ]$ and helices for $\theta = [0^\circ; 45^\circ]$ (Figure B.14). Similar to smaller size particles, the bigger particles form rings for $\theta = [60^\circ; 90^\circ]$ when the patches are located close to the particle equator. Random coils only form for $D/W = 5.0$ at high values of ϕ and θ where the patches are far apart. As their size increases, the coil region vanishes; and the particles tend to form either rings or helices. The absence of the coil region for $D/W > 4.0$ indicates that the particle size should exceed a certain threshold to stabilize the formation of helices for a given patch size. However, as the particle size increases, the ring region is also broadened particularly at high

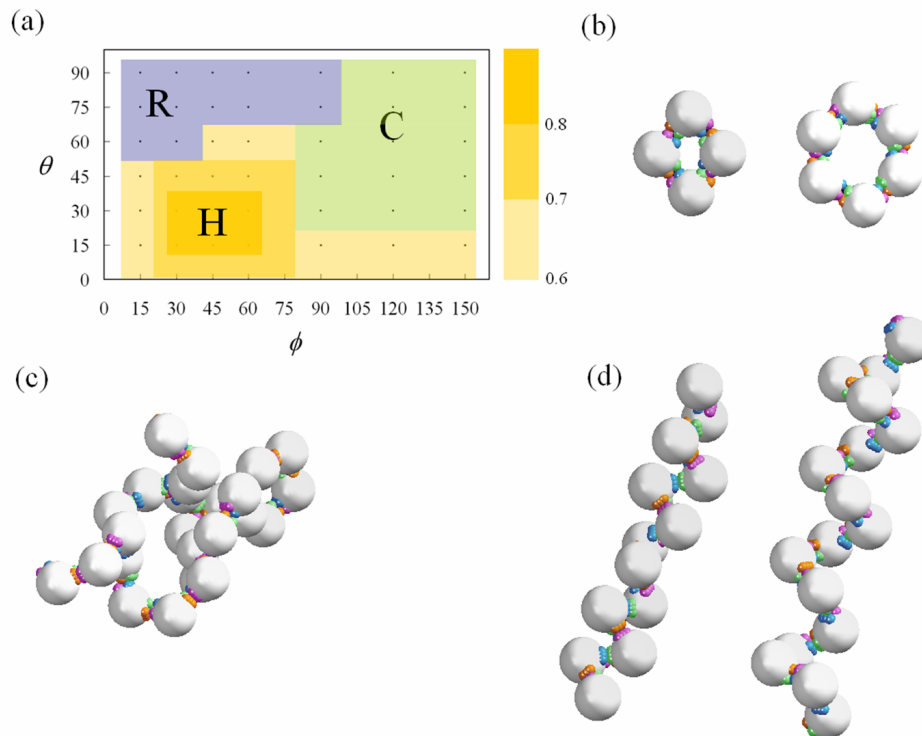


Figure B.13 (a) Energy landscape for patchy particles with $D/W = 4.0$. Rings (R), random coils (C) and helices (H) form depending on the patch arrangement. The legend on the right shows the frequency of occurrence of the helices. Example snapshots: (b) rings formed at $(\phi = 90^\circ; \theta = 0^\circ)$ (left) and $(\phi = 120^\circ; \theta = 60^\circ)$ (right); (c) a random coil formed at $(\phi = 120^\circ; \theta = 45^\circ)$; (d) helices formed at $(\phi = 30^\circ; \theta = 30^\circ)$ (left) and formed at $(\phi = 150^\circ; \theta = 0^\circ)$ (right).

ϕ and θ . This is because the imperfection in the patch aggregation, which is comparable to the helical pitch, allows the two chain ends to lock together. It is important to note that at $T^* = 0.25$, the assembled clusters are highly unlikely to dissolve or re-arrange once formed and thus suffer from kinetic traps. At higher temperatures ($0.25 \leq T^* \leq 0.67$), the helix region will be broadened because the particles are able to re-orient maximize their energetically favorable patch contacts.

The effects of θ with a given size ratio D/W and ϕ on the geometry of the helices are shown in Figure B.15. For $D/W = 5.0$ and $\phi = 120^\circ$, we observe that the helical radius increases with θ while the helical pitch fluctuates widely during the simulation. The angles used in Figure B.15 are those in the optimal range found in Figure B.14.

Meanwhile, for $D/W = 7.0$ and $\theta = 45^\circ$, the assembled helices are more well controlled by ϕ . We notice the monotonous increase in the helical radius and pitch as ϕ increases from 30° to 150° . Although the helices are also subject to thermal fluctuations, they seem to retain their shape better than varying θ .

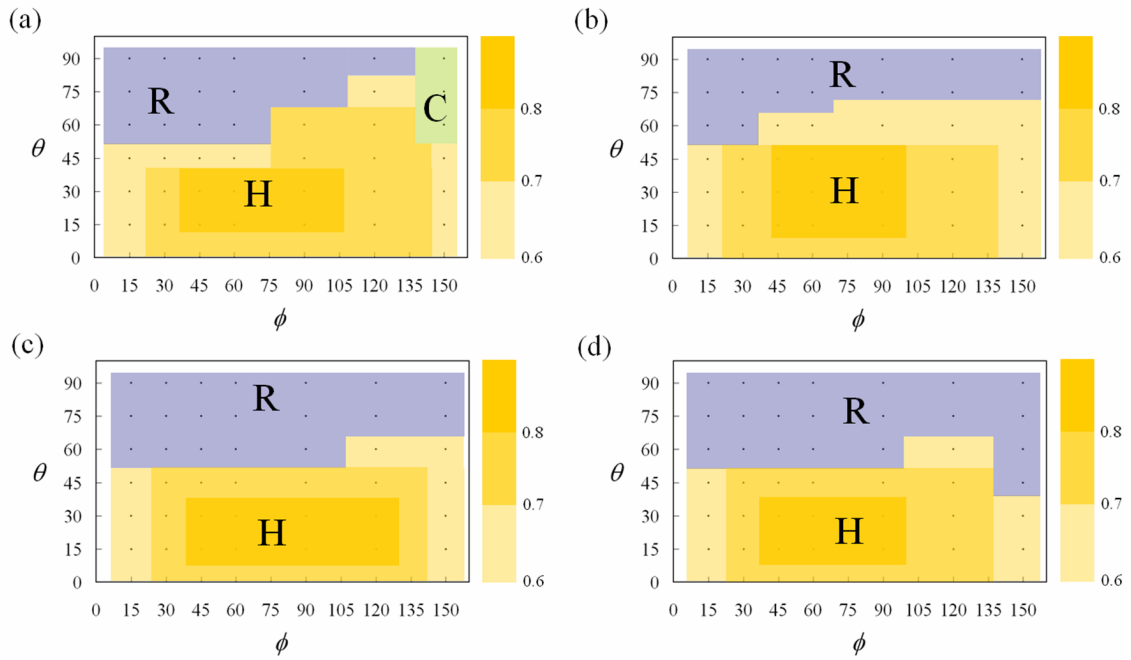


Figure B.14 Landscapes for different particle sizes (a) $D/W = 5.0$; (b) $D/W = 6.0$; (c) $D/W = 7.0$ and (d) $D/W = 8.0$. Rings (R), random coils (C) and helices (H) form depending on the patch arrangement. The boundaries are drawn to guide the eyes. The legend on the right shows the frequency of occurrence of the helices.

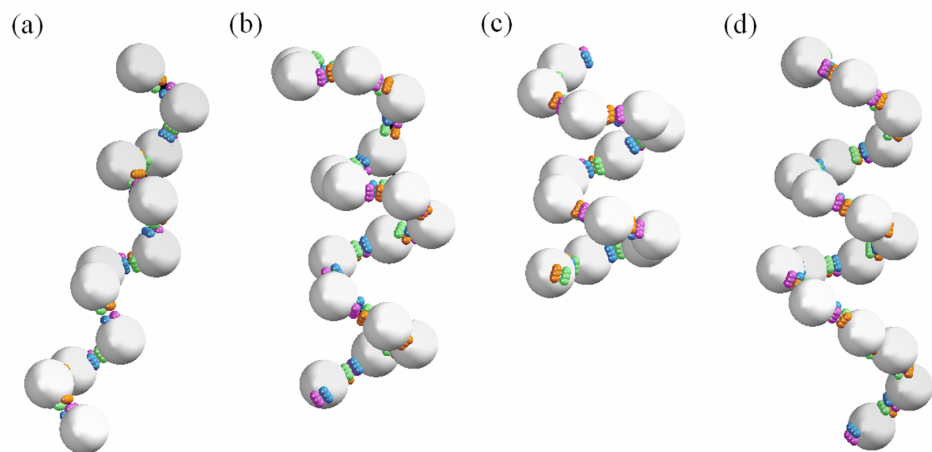


Figure B.15 Helices formed by patchy particles with $D/W = 5.0$ and $\theta = 120^\circ$: (a) $\theta = 0^\circ$; (b) $\theta = 45^\circ$; (c) $\theta = 75^\circ$ and (d) $\theta = 90^\circ$.

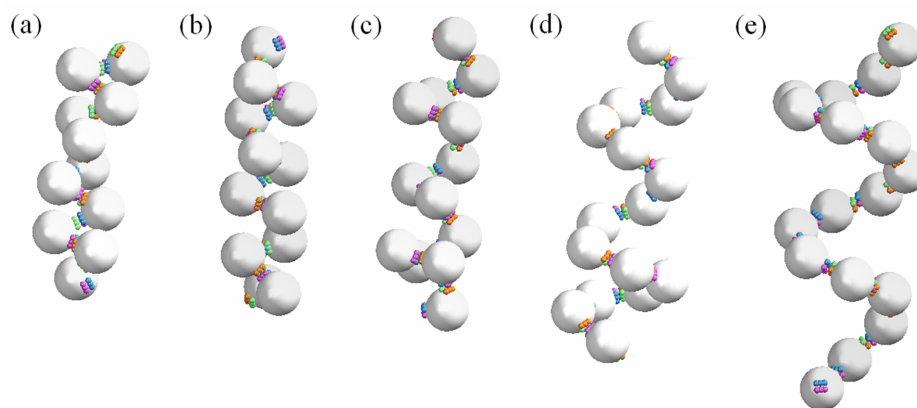


Figure B.16 Helices formed by patchy particles with $D/W = 7.0$ and $\theta = 45^\circ$: (a) $\phi = 30^\circ$; (b) $\phi = 60^\circ$; (c) $\phi = 90^\circ$; (d) $\phi = 120^\circ$; and (e) $\phi = 150^\circ$.

B.2.4 Conclusion and outlook

We have shown that patchy particles with two linear patches arranged in a non-planar fashion self-assemble into helical chains. The directional and selective interaction of the patches resemble the lock-and-key interaction between globular proteins, giving rise to the formation of helices whose the length scale is much greater than the building blocks themselves. The chirality of the building blocks leads to the unique handedness of the helical structures. We find that for a given particle size the helices are most likely to be observed in a certain range of the arrangement, represented by two angles (ϕ ; θ). Meanwhile, rings and random coils are competing kinetically trapped configurations. The focus of future study is to map the energy landscapes for different patch arrangements and particle size, which provide useful information on the robustness of engineering helical structures with a uniform chirality. We expect that this study would inspire the fabrication of such building blocks, aiming at an inorganic analogy of biological supramolecules.

Appendix C

VisualizerX visualization software

C.1 Introduction

We have been developing VisualizerX, a graphical user interface (GUI) software for visualizing 3-D molecular simulation data since 2006. VisualizerX is implemented using Microsoft® Visual C++®, Microsoft® Foundation Classes® (MFC) and OpenGL. The software requires Windows XP or later and at least 512MB RAM. The distribution package consists of the binary executable (VisualzerX.exe, 1.5MB) and MFC and OpenGL dynamic linked libraries (mfc42d.dll, mfco42d.dll, msvcrt.dll, msvcrtd.dll, msvcp60d.dll, glu32.dll, glut32.dll and opengl32.dll). Trial versions and user manual can be obtained by contacting the author at ndtrung@umich.edu.

In addition to the standard interface of a Windows application, the most powerful feature of VisualizerX is the user-defined template for drawing 3-D particles. Users can declare how to draw individual building blocks from primitive geometries in a text file and apply the template to the XYZ data. VisualizerX can be used with other visualization packages for further analysis. Most of the visual results in this thesis are obtained from VisualizerX.

C.2 Features

VisualizerX reads in the particle XYZ coordinates and shows them on the main window. As of version 1.10.00 VisualizerX offers the following features:

C.2.1 Visualization

- Flexible user-defined building block primitives: cylinders, polygons, polyhedra, spheres with different diameters, lines and more to be added if requested
- Overlay vectors (i.e. dipoles, velocities, accelerations) to individual particles

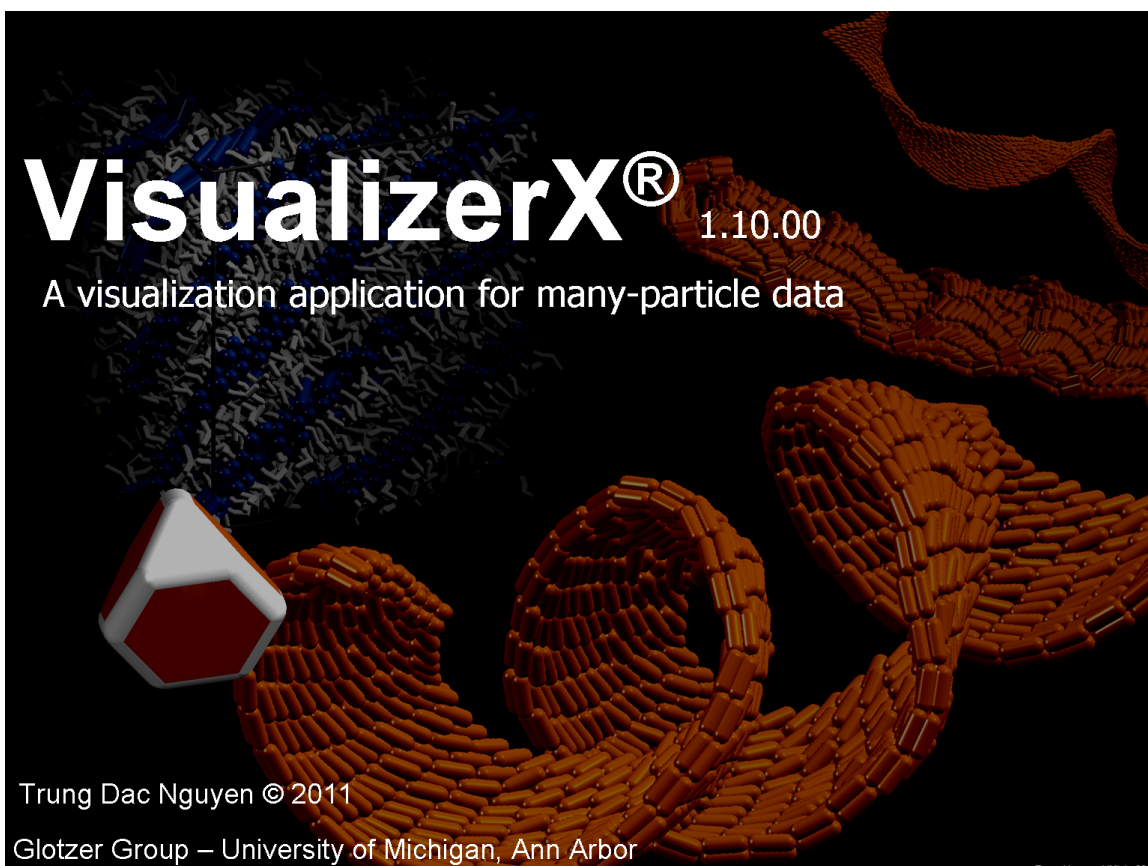


Figure C.1 VisualizerX 1.10.0 welcome screen

- Multiple views and multiple structures at the same time

C.2.2 Analysis

- Radial distribution function for specified atom types in 2-D and 3-D
- Bond order diagram for specified atom types and ranges
- Diffraction pattern for selected particles
- Filter particles based on region (box or sphere), types and indices
- Interactive manipulation
- Zoom, translate in and out, scaling, camera setup with mouse clicks
- Shift in X-, Y- and Z- directions with periodic boundary conditions
- Materials color can be adjusted interactively
- Special effects: lighting, blending, fogging and outlines
- Replicate selected particles

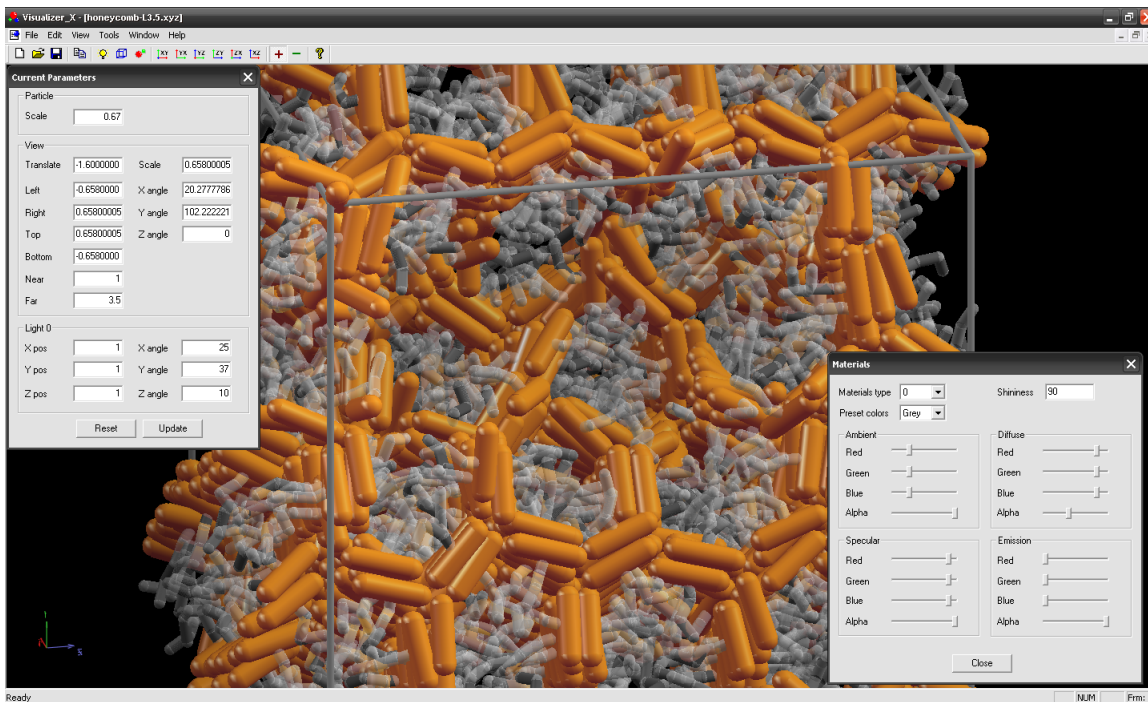


Figure C.2 Honeycomb structure formed by laterally tethered nanorods. Users can adjust viewing parameters, lighting conditions and materials colors interactively.

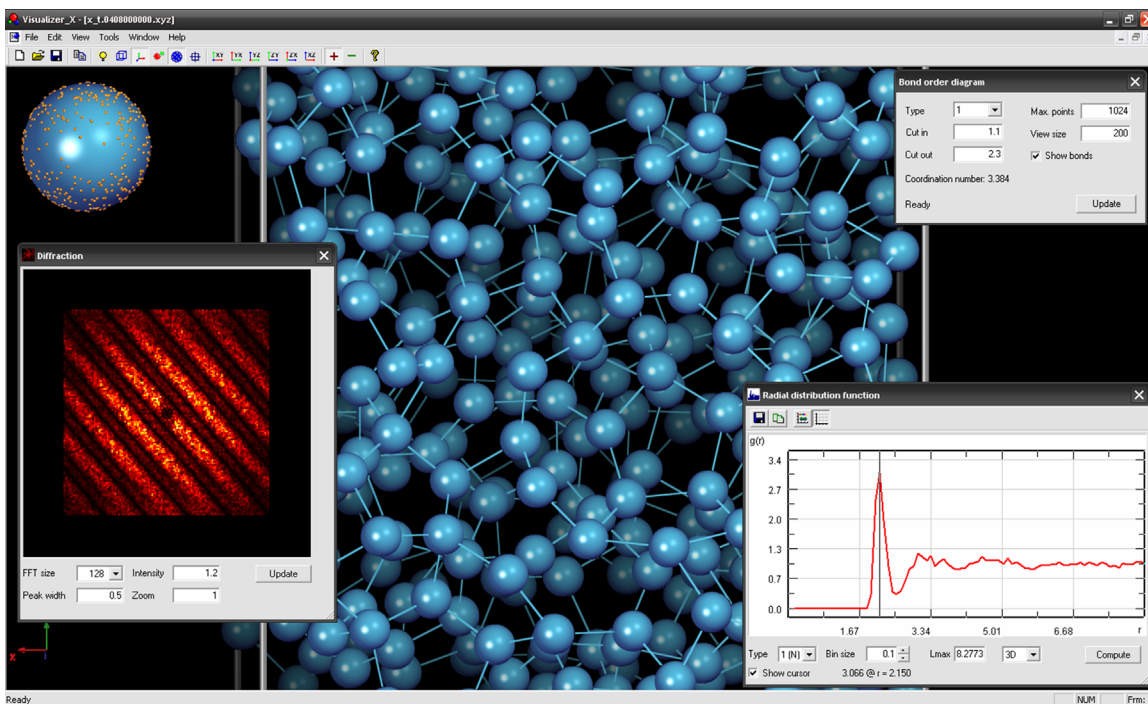


Figure C.3 Radial distribution function, bond order diagram and diffraction pattern of a quasicrystalline structure formed by "bumpy" soft tetrahedra. Only centers of mass are visualized. "Bonds" represent distances between particle centers at the first peak of the radial distribution function.

C.2.3 Input/Ouput

- Support drag-and-drop XYZ-format files directly to the main window
- Support Copy/Paste (Device Independent Bitmap- DIB) images into documents e.g. Microsoft®Office®and Paint®. Note that DIBs in PowerPoint can be saved as high resolution images (up to 300 dpi) with ExportBitmapResolution set in the Windows®registry. Higher DPIs can be achieved by GIMP
- Support streaming from ASCII files which are produced by concatenating multiple .XYZ files for animated visualization and screen-capture software
- Support streaming from standard input
- Support exporting to BMP images
- Support exporting to Encapsulated Post Script (EPS) files

C.3 Future development

In the future, the DCD data format and other image formats such as PNG and JPEG will be supported. Other special effects with lighting and refraction will be implemented. Functionalities can be further added to VisualizerX upon request.

Bibliography

1. W. J. Parak, T. Pellegrino, C. M. Micheel, D. Gerion, S. C. Williams, and A. P. Alivisatos. Conformation of oligonucleotides attached to gold nanocrystals probed by gel electrophoresis. *Nano Letters*, 3(1), 2003.
2. S. Westenhoff and N. A. Kotov. Quantum dot on a rope. *Journal of American Chemistry Society*, 124(11), 2004.
3. S. Sacanna, W. T. M. Irvine, P. M. Chaikin, and D. J. Pine. Lock and key colloids. *Nature*, 464:575578, 2010.
4. G. A. DeVries, M. Brunnbauer, Y. Hu, A. M. Jackson, B. Long, B. T. Neltner, O. Uzun, B. H. Wunsch, and F. Stellacci. Divalent metal nanoparticles. *Science*, 315:358–360, 2007.
5. Z. Nie, D. Fava, E. Kumacheva, S. Zou, G. C. Walker, and M. Rubinstein. Self-assembly of metalpolymer analogues of amphiphilic triblock copolymers. *Nature Materials*, 6:609, 2007.
6. B. Pan, L. Ao, F. Gao, H. Tian, R. He, and D. Cui. End-to-end self-assembly and colorimetric characterization of gold nanorods and nanospheres via oligonucleotide hybridization. *Nanotechnology*, 16:1776–1780, 2005.
7. K. Roh, D. C. Martin, and J. Lahann. Biphasic janus particles with nanoscale anisotropy. *Nature*, 4:759–763, 2005.
8. J. W. Ciszek, L. Huang, Y. Wang, and C. A. Mirkin. Kinetically controlled, shape-directed assembly of nanorods. *Small*, 4(2):206, 2008.
9. D. W. Lim, S. Hwang, O. Uzun, F. Stellacci, and J. Lahann. Compartmentalization of gold nanocrystals in polymer microparticles using electrohydrodynamic co-jetting. *Macromolecular Rapid Communications*, 31:176182, 2010.
10. T. Pellegrino, T. Liedl S. Kudera, A. M. Javier, L. Manna, and W. J. Parak. On the development of colloidal nanoparticles towards multifunctional structures and their possible use for biological applications. *Small*, 1(1):49, 2005.
11. V. F. Puntès, K. M. Krishnan, and A. P. Alivisatos. Colloidal nanocrystal shape and size control: The case of cobalt. *Science*, 291(5511):2115–2117, 2001.
12. S. Link, C. Burda, B. Nikoobakht, and M. A. El-sayed. Laser-induced shape changes of colloidal gold nanorods using femtosecond and nanosecond laser pulses. *Journal of Physical Chemistry B*, 104:6152–6153, 2000.
13. S. Link, Z. L. Wang, and M. A. El-sayed. How does a gold nanorod melt? *Journal of Physical Chemistry B*, 104(33):7867–7870, 2000.
14. S. Srivastava, A. Santos, K. Critchley, K.-S. Kim, P. Podsiadlo, K. Sun, J. Lee, C. Xu, G. D. Lilly, S. C. Glotzer, and N. A. Kotov. Light-controlled self-assembly of semiconductor nanoparticles into twisted ribbons. *Science*, 327:1355–1359, 2010.

15. Z. L. Zhang and S. C. Glotzer. Tethered nano building blocks: Toward a conceptual framework for nanoparticle self-assembly. *Nano Letters*, 3(10):1341–1346, 2003.
16. M. A. Horsch, C. R. Iacovella, Z. Zhang, and S. C. Glotzer. Self-organization of nanoscopic building blocks into ordered assemblies. *Materials Research Society Symposium Proceedings*, 818, 2004.
17. M. A. Horsch, Z. Zhang, and S. C. Glotzer. Self-assembly of polymer-tethered nanorods. *Physical Review Letters*, 95:056105, 2005.
18. M. A. Horsch, Z. Zhang, and S. C. Glotzer. Self-assembly of laterally-tethered nanorods. *Nano Letters*, 6:2406, 2006.
19. M. A. Horsch, Z. Zhang, and S. C. Glotzer. Simulation studies of self-assembly of end-tethered nanorods in solution and role of rod aspect ratio and tether length. *Journal of Chemical Physics*, 125:184903–12, 2006.
20. E. R. Chan, X. Zhang, C. Y. Lee, M. Neurock, and S. C. Glotzer. Simulations of tetra-tethered organic/inorganic nanocube-polymer assemblies. *Macromolecules*, 38(14):6168–6180, 2005.
21. X. Zhang, E. R. Chan, and S. C. Glotzer. Self-assembled morphologies of monotethered polyhedral oligomeric silsesquioxane nanocubes from computer simulation. *Journal of Chemical Physics*, 123:184718–6, 2005.
22. N. A. Kotov. *Nanoparticle Assemblies and Superstructures*. CRC Press, 2005.
23. L. Manna, E. C. Scher, and A. P. Alivisatos. Synthesis of soluble and processable rod-, arrow-, teardrop-, and tetrapod-shaped cdse nanocrystals. *J. Am. Chem. Soc.*, 122:12700–12706, 2000.
24. Z. Tang, Y. Wang, S. Shanbhag, M. Giersig, and N. A. Kotov. Spontaneous transformation of cdte nanoparticles into angled te nanocrystals: From particles and rods to checkmarks, x-marks, and other unusual shapes. *Journal of American Chemistry Society*, 128, 2006.
25. S. C. Glotzer and M. J. Solomon. Anisotropy of building blocks and their assembly into complex structures. *Nature Materials*, 6:557–562, 2007.
26. C. R. Iacovella, M. A. Horsch, and S. C. Glotzer. Local ordering of polymer-tethered nanospheres and nanorods. *Journal of Chemical Physics*, 129(044902-10), 2008.
27. Z. L. Zhang and S. C. Glotzer. Self-assembly of patchy particles. *Nano Letters*, 4:1407–1413, 2004.
28. E. G. Noya, C. Vega, J. P. K. Doye, and A. A. Louis. Phase diagram of model anisotropic particles with octahedral symmetry. *arXiv:0706.0650v1*, 2007.

29. A. W. Wilber, J. P. K. Doye, A. A. Louisa, E. G. Noya, M. A. Miller, and P. Wong. Reversible self-assembly of patchy particles into monodisperse icosahedral clusters. *Journal of Chemical Physics*, 127:085106, 2007.
30. S. Hormoz and M. P. Brenner. Design principles for self-assembly with short-range interactions. *Proceedings of the National Academy of Sciences of the United States of America*, www.pnas.org/cgi/doi/10.1073/pnas.1014094108, 2011.
31. E. Jankowski and S. C. Glotzer. Assembly pathway engineering: designing patchy particles for self-assembly propensity. *Preprint*, 11.
32. S. Torquato. Inverse optimization techniques for targeted self-assembly. *Soft Matter*, 5:11571173, 2009.
33. S. C. Glotzer, M. A. Horsch, C. R. Iacovella, Z. Zhang, E. R. Chan, and X. Zhang. Self-assembly of anisotropic tethered nanoparticle shape amphiphiles. *Current Opinion in Colloid and Interface Science*, 10:287, 2005.
34. C. R. Iacovella, M. A. Horsch, Z. L. Zhang, and S. C. Glotzer. Phase diagrams of self-assembled mono-tethered nanospheres from molecular simulation and comparison to surfactants. *Langmuir*, 21:9488, 2005.
35. C. R. Iacovella and S. C. Glotzer. Phase behavior of ditethered nanospheres. *Soft Matter*, 5:4492–4498, 2009.
36. C. R. Iacovella and S. C. Glotzer. Complex crystal structures formed by the self-assembly of ditethered nanospheres. *Nano Letters*, 9(3):1206–1211, 2009.
37. Z. L. Zhang, Z. Tang, N. A. Kotov, and S. C. Glotzer. Simulations and analysis of self-assembly of cdte nanoparticles into wires and sheets. *Nano Letters*, 7:1670–1675, 2007.
38. T. D. Nguyen, Z. L. Zhang, and S. C. Glotzer. Molecular simulation study of self-assembly of tethered v-shaped nanoparticles. *Journal of Chemical Physics*, 129:244903–11, 2008.
39. M. J. Solomon. Directions for targeted self-assembly of anisotropic colloids from statistical thermodynamics. *Current Opinion in Colloid and Interface Science*, page doi: 10.1016/j.cocis.2011.006, 2011.
40. X. Peng, Mi Yan, and H. Ge. Effects of magnetic field gradient on particle distributions of suspension comprised of both magnetic and nonmagnetic particles using two-dimensional monte carlo simulations. *Advanced materials research*, 79:1301–1304, 2009.
41. J. P. Singh, P. P. Lele, F. Nettesheim, N. J. Wagner, and E. M. Furst. One- and two-dimensional assembly of colloidal ellipsoids in ac electric fields. *Physical Review E*, 79:050401–4, 2009.

42. E. V. Shevchenko, D. V. Talapin, N. A. Kotov, S. O'Brien, and C. B. Murray. Structural diversity in binary nanoparticle superlattices. *Nature*, 439:55–59, 2006.
43. D. V. Talapin, J. S. Lee, M. V. Kovalenko, and E. V. Shevchenko. Prospects of colloidal nanocrystals for electronic and optoelectronic applications. *Chemical Review*, 110(1):389458, 2010.
44. G. von Freymann, A. Ledermann, M. Thiel, I. Staude, S. Essig, K. Busch, and M. Wegener. Three-dimensional nanostructures for photonics. *Advanced Functional Materials*, 20(7):1038–1052, 2010.
45. H. Yan, S. H. Park, G. Finkelstein, J. H. Reif, and T. H. LaBean. Dna templated self-assembly of protein arrays and highly conductive nanowires. *Science*, 301:1882, 2003.
46. V. I. Kopp and A. Z. Genack. Double-helix chiral fibers. *Optics Letters*, 28:1876, 2003.
47. V. I. Kopp, Z. Q. Zhang, and A. Z. Genack. Lasing in chiral photonic structures. *Progress in Quantum Electronics*, 27:369, 2003.
48. C. Tschierske. Liquid crystal engineering new complex mesophase structures and their relations to polymer morphologies, nanoscale patterning and crystal engineering. *Chemical Society Reviews*, 36:19301970, 2007.
49. J.-M. Nam, C. Shad Thaxton, and C. A. Mirkin. Nanoparticle-based bio-bar codes for the ultrasensitive detection of proteins. *Science*, 301(5641):1884–1886, 2003.
50. M. Ferrari. Nanogeometry: Beyond drug delivery. *Nature Nanotechnology*, 3:131 – 132, 2008.
51. J. N. Israelachvili. *Intermolecular and surface forces, Third Edition*. Academic Press, 2011.
52. S. C. Glotzer, M. Solomon, and N. Kotov. Self-assembly: From nanoscale to microscale colloids. *AIChE Journal*, 50:2978, 2004.
53. K. J. M. Bishop, C. E. Wilmer, S. Soh, and B. A. Grzybowski. Nanoscale forces and their uses in self-assembly. *Small*, 5(14):1600–1630, 2009.
54. D. J. Weeks, D. Chandler, and H. C. Andersen. Role of repulsive forces in forming the equilibrium structure of simple liquids. *Journal of Chemical Physics*, 54:5237–5247, 1971.
55. H. R. Warner. Kinetic-theory and rheology of dilute suspensions of finitely extendible dumbbells. *Industrial and Engineering Chemistry Fundamentals*, 11:379–387, 1972.
56. M. P. Allen and D. J. Tildesley. *Computer simulations of liquids*. Oxford University Press, USA, 1989.

57. D. Frenkel and B. Smit. *Understanding Molecular Simulation From Algorithms to Applications*. Academic Press, 2002.
58. D. A. McQuarrie. *Statistical Mechanics*. University Science Books, 2000.
59. J. B. Marion and S. T. Thornton. *Classical Dynamics of Particles and Systems*. Saunders College Publishing, 1995.
60. M. A. Horsch, Z. L. Zhang, C. R. Iacovella, and S. C. Glotzer. Hydrodynamics and microphase ordering in block copolymers: Are hydrodynamics required for ordered phases with periodicity in more than one dimension? *Journal of Chemical Physics*, 121(22):11455–11462, 2004.
61. DLPOLY. Dlpoly, 2010.
62. NAMD. <http://www.ks.uiuc.edu/research/namd/>.
63. LAMMPS. <http://lammmps.sandia.gov/>.
64. HOOMD-blue. <http://codeblue.umich.edu/hoomd-blue/>, 2010.
65. W. L. Jorgensen, J. Chandrasekhar, J. D. Madura, R. Impey, and M. L. Klein. Comparison of simple potential functions for simulating liquid water. *Journal of Chemical Physics*, 79:926–935, 1983.
66. S. Miyamoto and P. A. Kollman. An analytical version of the shake and rattle algorithm for rigid water models. *Journal of Computational Chemistry*, 13(8):952–962, 1992.
67. T. R. Forester and W. Smith. Shake, rattle, and roll: Efficient constraint algorithms for linked rigid bodies. *Journal of Computational Chemistry*, 19(1):102–111, 1998.
68. D. Dubbeldam, G. A. E. Oxford, R. Krishna, L. J. Broadbelt, and R. Q. Snurr. Distance and angular holonomic constraints in molecular simulations. *Journal of Chemical Physics*, 133:034114–15, 2010.
69. D. J. Evans. On the representation of orientation space. *Molecular Physics*, 34:317–325, 1977.
70. T. F. Miller III, M. Eleftheriou, P. Pattnaik, A. Ndirango, D. Newns, and G. J. Martyna. Symplectic quaternion scheme for biophysical molecular dynamics. *Journal of Chemical Physics*, 116(20):8649–8659, 2002.
71. S. Plimpton. Fast parallel algorithms for short-range molecular dynamics. *Journal of Computational Physics*, 117:1, 1995.
72. J. A. Anderson, C. D. Lorenz, and A. Travesset. General purpose molecular dynamics simulations fully implemented on graphics processing units. *Journal of Computational Physics*, 227:5342, 2008.

73. T. D. Nguyen, C. L. Phillips, J. A. Anderson, and S. C. Glotzer. Rigid body constraints realized in massively parallel molecular dynamics on graphics processing units. *submitted*.
74. X. Zhang, Z. L. Zhang, and S. C. Glotzer. Simulation study of cyclic-tethered nanocube self-assemblies: Effect of tethered nanocube architectures. *Nanotechnology*, 18(11):115706–6, 2007.
75. M. A. Horsch, Z. Zhang, and S. C. Glotzer. Self-assembly of end-tethered nanorods in a neat system and role of block fractions and aspect ratio. *Soft Matter*, 6:945954, 2010.
76. T. D. Nguyen and S. C. Glotzer. Switchable helical structures formed by the hierarchical self-assembly of laterally-tethered nanorods. *Small*, 5(18):2092–2096, 2009.
77. T. D. Nguyen and S. C. Glotzer. Reconfigurable assemblies of shape-changing nanorods. *ACS Nano*, 4(5):2584–2594, 2010.
78. D. R. Heine, M. K. Petersen, and G. S. Grest. Effect of particle shape and charge on bulk rheology of nanoparticle suspensions. *Journal of Chemical Physics*, 132:184509–6, 2010.
79. J. Elliott and A. Windle. A dissipative particle dynamics method for modeling the geometrical packing of filler particles in polymer composites. *Journal of Chemical Physics*, 113:10367–10376, 2000.
80. R. Mountain. Solvation structure of ions in water. *International Journal of Thermophysics*, 28:536–543, 2007.
81. S. D. Johnson, R. D. Mountain, and P. H. E. Meijer. Simulation of c-60 through the plastic transition temperatures. *Journal of Chemical Physics*, 103:1106–1108, 1995.
82. E. Bitzek, P. Koskinen, F. Gahler, M. Moseler, and P. Gumbsch. Structural relaxation made simple. *Physical Review Letters*, 97:170201–4, 2006.
83. J. M. Troyer and F. E. Cohen. Protein conformational landscapes: energy minimization and clustering of a long molecular dynamics trajectory. *Proteins*, 23:97–110, 1995.
84. W. H. Press, B. P. Flannery, S. A. Teukolsky, and W. T. Vetterling. *Numerical Recipes in C*. Cambridge University Press, 1997.
85. NVIDIA. <http://www.nvidia.com/object/>, 2010.
86. H. Kamberaj, R. J. Low, and M. P. Neal. Time reversible and symplectic integrators for molecular dynamics simulations of rigid molecules. *Journal of Chemical Physics*, 122:224114, 2005.
87. N. S. Martys and R. D. Mountain. Velocity verlet algorithm for dissipative-particle-dynamics-based models of suspensions. *Physical Review E*, 59(3):3733–3736, 1999.

88. A. Haji-Akbari, M. Engel, A. S. Keys, X. Y. Zheng, R. Petschek, P. Palfy-Muhoray, and S. C. Glotzer. Disordered, quasicrystalline and crystalline phases of densely packed tetrahedra. *Nature*, 462:773–777, 2009.
89. M. Kroger. Simple models for complex nonequilibrium fluids. *Physics Reports*, 390:453–551, 2004.
90. V. L. Lorman and B. Mettout. Theory of chiral periodic mesophases formed from an achiral liquid of bent-core molecules. *Physical Review E*, 69:061710, 2004.
91. T. C. Lubensky and L. Radzihovsky. Theory of bent-core liquid-crystal phases and phase transitions. *Physical Review E*, 66:031704, 2002.
92. I. Dozov. On the spontaneous symmetry breaking in the mesophases of achiral banana-shaped molecules. *Europhysics Letters*, 56(2):247–253, 2001.
93. V. Pryamitsyn and V. Ganesan. Self-assembly of rodcoil block copolymers. *Journal of Chemical Physics*, 120(12):5824–5838, 2004.
94. T. Niori, T. Sekine, J. Watanabe, T. Furukawab, and H. Takezoe. Distinct ferroelectric smectic liquid crystals consisting of banana shaped achiral molecules. *Journal of Materials Chemistry*, 6(7):1231–1233, 1996.
95. Y. Maedaa, T. Niori, J. Yamamoto, and H. Yokoyama. Phase behavior of banana-shaped molecules under pressure. *Thermochimica Acta*, 431:87–93, 2005.
96. P. Pyc, J. Mieczkowski, D. Pocięcha, E. Gorecka, B. Donnio, and D. Guillon. Bent-core molecules with lateral halogen atoms forming tilted, synclitic and anticlitic, lamellar phases. *Journal of Materials Chemistry*, 14:2374–2379, 2004.
97. K. Pelz, W. Weissflog, U. Baumeister, and S. Diele. Various columnar phases formed by bent-core mesogens. *Liquid Crystals*, 30(10):1151–1158, 2003.
98. R. A. Reddy, B. K. Sadashiva, and V. A. Raghunathan. Banana-shaped mesogens derived from 2,7-dihydroxynaphthalene and 1,3-dihydroxybenzene: Novel columnar mesophases. *Chemistry of Materials*, 16(21):4050–4062, 2004.
99. C. Keith, R. A. Reddy, M. Prehm, U. Baumeister, H. Kresse, J. L. Chao, H. Hahn, H. Lang, and C. Tschierske. Layer frustration, polar order and chirality in liquid crystalline phases of silyl-terminated achiral bent-core molecules. *Chemistry-A European Journal*, 13:2556–2577, 2007.
100. F. C. Yu and L. J. Yu. Mesophases of achiral bent molecules. *Chemistry of Materials*, 18(23):5410–5420, 2006.
101. J. Thisayukta, H. Takezoe, and J. Watanabe. Study on helical structure of the b4 phase formed from achiral banana-shaped molecule. *Japan Journal of Applied Physics*, 40:3277–3287, 2001.

102. G. Liao, I. Shashikala, C. V. Yelamaggad, D. S. Shankar Rao, S. Krishna Prasad, and A. J. Jkli. Ferroelectricity of a bent-core material with cholesteryl terminal chain. *Physical Review E*, 73:051701, 2006.
103. G. Pelzl, M. W. Schroder, U. Dunemann, S. Diele, W. Weissflog, C. Jones, D. Coleman, N. A. Clark, R. Stannarius, J. Li, B. Dasc, and S. Grande. The first bent-core mesogens exhibiting a dimorphism b7smcpa. *Journal of Materials Chemistry*, 14:2492–2598, 2004.
104. S. Diele, S. Grande, H. Kruth, C. H. Lischka, G. Pelzl, W. Weissflog, and I. Wirth. Structure and properties of liquid crystalline phases formed by achiral banana-shaped molecules. *Ferroelectrics*, 212, 1998.
105. W. Weissflog, H. N. S. Murthy, S. Diele, and G. Pelzl. Relationships between molecular structure and physical properties in bent-core mesogens. *Philosophical Transactions of Royal Society A*, 364:2657–2679, 2006.
106. F. Araoka, N.Y. Ha, Y. Kinoshita, B. Park, J. W. Wu, and H. Takezoe. Twist-grain-boundary structure in the b4 phase of a bent-core molecular system identified by second harmonic generation circular dichroism measurement. *Physical Review Letters*, 94:137801, 2005.
107. H. Niwano, M. Nakata, J. Thisayukta, D. R. Link, H. Takezoe, and J. Watanabe. Chiral memory on transition between the b2 and b4 phases in an achiral banana-shaped molecular system. *Journal of Physical Chemistry B*, 108:14889–14896, 2004.
108. C. L. Folcia, J. Etxebarria, J. Ortega, and M. B. Ros. Structure of mesogens possessing b7 textures: The case of the bent-core mesogen 8-opimb-no2. *Physical Review E*, 72:041709, 2005.
109. B. A. Parviz, D. Ryan, and G. M. Whitesides. Using self-assembly for the fabrication of nanoscale electronic and photonic devices. *IEEE Transactions on Advanced Packaging*, 26(3):233–241, 2003.
110. V. Veselago, L. Braginsky, V. Shklover, and C. Hafner. Negative refractive index materials. *Journal of Computational and Theoretical Nanoscience*, 3:1–30, 2006.
111. V. Yannopoulos. Negative index of refraction in artificial chiral materials. *Journal of Physics: Condensed Matter*, 18:68836890, 2006.
112. Q. Cheng and T. J. Cui. Negative refractions in uniaxially anisotropic chiral media. *Physical Review B*, 73:113104, 2006.
113. D. R. Link, G. Natale, R. Shao, J. E. Maclennan, N. A. Clark, E. Korblova, D. M. Walba, L. Eshdat, E. Korblova, and R. K. Shoemaker. Spontaneous formation of macroscopic chiral domains in a fluid smectic phase of achiral molecules. *Science*, 278:1924 – 1927, 1997.
114. J. Pendry. A chiral route to negative refraction. *Science*, 306:1353–1355, 2004.

115. R. Memmer. Liquid crystal phases of achiral banana-shaped molecules: a computer simulation study. *Liquid Crystals*, 29(4):483–496, 2002.
116. S. J. Johnston, R. J. Low, and M. P. Neal. Computer simulation of apolar bent-core and rodlike molecules. *Physical Review E*, 65:051706, 2002.
117. S. J. Johnston, R. J. Low, and M. P. Neal. Computer simulation of polar bent-core molecules. *Physical Review E*, 66:061702, 2002.
118. W. Jozefowicz and L. Longa. Frustration in smectic layers of polar gay-berne systems. *Physical Review E*, 76, 2007.
119. P. Grzybowski and L. Longa. Gay-berne models of bent-core systems and stability of biaxial nematic phase. *in press*, 2008.
120. J. Xu, R. L. B. Selinger, J. V. Selinger, and R. Shashidhar. Monte carlo simulation of liquid-crystal alignment and chiral symmetry-breaking. *Journal of Chemical Physics*, 115(9):4333–4338, 2001.
121. A. Dewar and P.J. Camp. Computer simulations of bent-core liquid crystals. *Physical Review E*, 70:011704, 2004.
122. A. Dewar and P. J. Camp. Dipolar interactions, molecular flexibility, and flexoelectricity in bent-core liquid crystals. *Journal of Chemical Physics*, 123(17):174907, 2005.
123. T. Soddemann, B. Dunweg, and K. Kremer. A generic computer model for amphiphilic systems. *European Physical Journal E*, 6:409, 2002.
124. G. S. Grest and K. Kremer. Molecular dynamics simulations for polymers in the presence of a heat bath. *Physical Review A*, 33:3628, 1986.
125. K. E. Sung, S. A. Vanapalli, D. Mukhija, H. McKay, J. M. Millunchick, M. A. Burns, and M. J. Solomon. Programmable fluidic production of microparticles with configurable anisotropy. *Journal of American Chemistry Society*, 130(4):1335 –1340, 2008.
126. S. A. Vanapalli, C. R. Iacovella, K. E. Sung, D. Mukhija, J. M. Millunchick, M. A. Burns, S. C. Glotzer, and M. J. Solomon. Fluidic assembly and packing of microspheres in confined channels. *Langmuir*, 24(7):3661, 2008.
127. E. Gorecka, D. Pocięcha, J. Mieczkowski, J. Matraszek, D. Guillon, and B. Donnio. Axially polar columnar phase made of polycatenar bent-shaped molecules. *Journal of American Chemistry Society*, 126(49):15946 –15947, 2004.
128. Y. Lansac, P. K. Maiti, N. A. Clark, and M. A. Glaser. Phase behavior of bent-core molecules. *Physical Review E*, 67:011703, 2003.

129. D. J. Hong, E. Lee, H. Jeong, J. Lee, W.-C. Zin, T. D. Nguyen, S. C. Glotzer, and M. Lee. Solid-state scrolls from hierarchical self-assembly of t-shaped rodcoil molecules. *Angewandte Chemie International Edition*, 48:1664, 2009.
130. C. Tschierske. Micro-segregation, molecular shape and molecular topology partners for the design of liquid crystalline materials with complex mesophase morphologies. *Journal of Materials Chemistry*, 11:2647-2671, 2001.
131. R. A. Reddy and C. Tschierske. Bent-core liquid crystals: Polar order, superstructural chirality and spontaneous desymmetrisation in soft matter systems. *Journal of Materials Chemistry*, 16:907-961, 2006.
132. B. Abu-Sharkh and A. AlSunaidi. Morphology and conformation analysis of self-assembled triblock copolymer melts. *Macromolecular Theory and Simulations*, 15:5075-15, 2006.
133. Y. Xia, T. D. Nguyen, M. Yang, P. Podsiadlo, B. Lee, A. Santos, Z. Tang, S. C. Glotzer, and N. A. Kotov. Self-assembly of virus-like self-limited supraparticles from inorganic nanoparticles. *Submitted*.
134. Z. Tang, N. A. Kotov, and M. Giersig. Spontaneous organization of single CdTe nanoparticles into luminescent nanowires. *Science*, 297:237-240, 2002.
135. S. Sun, C. B. Murray, D. Weller, L. Folks, and A. Moser. Monodisperse FePt nanoparticles and ferromagnetic FePt nanocrystal superlattices. *Science*, 287:1989-1992, 2000.
136. B. Nikoobakht, Z. L. Wang, and M. A. El-Sayed. Self-assembly of gold nanorods. *Journal of Physical Chemistry B*, 104:8635-8640, 2000.
137. Y. Sun and Y. Xia. Shape-controlled synthesis of gold and silver nanoparticles. *Science*, 298:2176-2179, 2002.
138. H. Colfen and S. Mann. Higher-order organization by mesoscale self-assembly and transformation of hybrid nanostructures. *Angewandte Chemie International Edition*, 42:2350-2365, 2003.
139. D. V. Talapin, E. V. Shevchenko, C. B. Murray, A. Kornowski, S. Frster, and H. Weller. CdSe and CdSe/Cds nanorod solids. *Journal of the American Chemical Society*, 126:12984-12988, 2004.
140. M. Niederberger and H. Colfen. Oriented attachment and mesocrystals: non-classical crystallization mechanisms based on nanoparticle assembly. *Physical Chemistry Chemical Physics*, 8:3271-3287, 2006.
141. S. Yang and L. Gao. Controlled synthesis and self-assembly of CeO₂ nanocubes. *Journal of the American Chemical Society*, 128:9330-9331, 2006.

142. J. S. Lee, E. V. Shevchenko, and D. V. Talapin. Au-pbs core-shell nanocrystals: plasmonic absorption enhancement and electrical doping via intra-particle charge transfer. *Journal of the American Chemical Society*, 130:9673–9675, 2008.
143. Z. Zhuang, Q. Peng, B. Zhang, and Y. Li. Controllable synthesis of cu₂s nanocrystals and their assembly into a superlattice. *Journal of the American Chemical Society*, 130:10482–10483, 2008.
144. A. Dong, J. Chen, P. M. Vora, J. M. Kikkawa, and C. B. Murray. Binary nanocrystal superlattice membranes self-assembled at the liquid-air interface. *Nature Materials*, 466:474–477, 2010.
145. M. R. Jones, R. J. Macfarlane, B. Lee, J. Zhang, K. L. Young, A. J. Senesi, and C. A. Mirkin. Dna-nanoparticle superlattices formed from anisotropic building blocks. *Nature Materials*, 9:913–917, 2010.
146. Z. Quan and J. Fang. Superlattices with non-spherical building blocks. *Nano Today*, 5:390–411, 2010.
147. M. P. Pileni. Nanocrystal self-assemblies: fabrication and collective properties. *Journal of Physical Chemistry B*, 105:3358–3371, 2001.
148. M. M. Maye, J. Luo, S. Lim, L. Han, N. N. Kariuki, D. Rabinovich, T. Liu, and C. J. Zhong. Size-controlled assembly of gold nanoparticles induced by a tridentate thioether ligand. *Journal of the American Chemical Society*, 125:9906–9907, 2003.
149. J. Zhuang, H. Wu, Y. Yang, and Y. C. Cao. Supercrystalline colloidal particles from artificial atoms. *Journal of the American Chemical Society*, 129:14166–14167, 2007.
150. K. Liu, Z. Nie, N. Zhao, W. Li, M. Rubinstein, and E. Kumacheva. Step-growth polymerization of inorganic nanoparticles. *Science*, 329:197–200, 2010.
151. M. G. Warner and J. E. Hutchison. Linear assemblies of nanoparticles electrostatically organized on dna scaffolds. *Nature Materials*, 2:272–277, 2003.
152. M. Manchester and N. F. Steinmetz. *Viruses and Nanotechnology*. Springer, Berlin Heidelberg, 2009.
153. D. L. Feldheim and C. A. Foss. *Metal nanoparticles: synthesis, characterization, and applications*. Marcel-Dekker, New York, 2002.
154. T. Chen, Z. L. Zhang, and S. C. Glotzer. A precise packing sequence for self-assembled convex structures. *Proceedings of the National Academy of Sciences of the United States of America*, 104,:717–722 (.), 2007.
155. L. Hong, A. Cacciuto, E. Luijten, and S. Granick. Clusters of amphiphilic colloid spheres. *Langmuir*, 24:621, 2008.
156. H. M. Keizer and R. P. Sijbesma. Hierarchical self-assembly of columnar aggregates. *Chemical Society Reviews*, 34:226, 2005.

157. T. Shimizu. Molecular self-assembly into one-dimensional nanotube architectures and exploitation of their functions. *Bulletin of Chemical Society of Japan*, 81(12):1554, 2008.
158. C. Giordano, M. T. Todaro, A. Salhi, L. Martiradonna, I. Viola, A. Passab, L. Carbone, G. Gigli, A. Passaseo, and M. De Vittorio. Nanocrystals cylindrical microcavities exploiting thin-walled ingaas/gaas microtubes. *Microelectronic Engineering*, 84:1408, 2007.
159. R. Ma, Y. Bando, and T. Sasaki. Directly rolling nanosheets into nanotubes. *Journal of Physical Chemistry B*, 108:2115, 2004.
160. M. Zhong, M. Zheng, L. Ma, and Y. Li. Self-assembly of versatile tubular-like In_2O_3 nanostructures. *Nanotechnology*, 18:465605, 2007.
161. O. G. Schmidt and K. Eberl. Thin solid films roll up into nanotubes. *Nature*, 410:168, 2001.
162. R. Songmuang, Ch. Deneke, and O. G. Schmidt. Rolled-up micro- and nanotubes from single-material thin films. *Applied Physics Letters*, 89:223109, 2006.
163. F. Giulieri and M. P. Krafft. Tubular microstructures made from nonchiral single-chain fluorinated amphiphiles: Impact of the structure of the hydrophobic chain on the rolling-up of bilayer membrane. *Journal of Colloid and Interface Science*, 258:335, 2003.
164. W. Y. Yang, E. Lee, and M. Lee. Tubular organization with coiled ribbon from amphiphilic rigid-flexible macrocycle. *Journal of American Chemical Society*, 128:3484, 2006.
165. Y. Chen, B. Zhu, F. Zhang, Y. Han, and Z. Bo. Hierarchical supramolecular self-assembly of nanotubes and layered sheets. *Angewandte Chemie International Edition*, 47(32):6015, 2008.
166. E. Lee, J. K. Kim, and M. Lee. Reversible scrolling of two-dimensional sheets from self-assembly of laterally-grafted amphiphilic rods. *Angewandte Chemie International Edition*, 48(20):3657, 2009.
167. J. K. Lim, J. W. Ciszek, F. Huo, J.-W. Jang, S. Hwang, and C. A. Mirkin. Actuation of self-assembled two component rod-like nanostructures. *Nano Letters*, 8(12):4441, 2008.
168. Z. Tian, H. Li, M. Wang, A. Zhang, and Z. Feng. Vesicular and tubular structures prepared from self-assembly of novel amphiphilic aba triblock copolymers in aqueous solutions. *Journal of Polymer Science Part A- Polymer Chemistry*, 46(3):1042, 2008.
169. L. Cheng, G. Zhang, L. Zhu, D. Chen, and M. Jiang. Nanoscale tubular and sheet-like superstructures from hierarchical self-assembly of polymeric janus particles. *Angewandte Chemie International Edition*, 47(52):10171, 2008.

170. S. Zhang, D. M. Marini, W. Hwang, and S. Santoso. Design of nanostructured biological materials through self-assembly of peptides and proteins. *Current Opinion in Chemical Biology*, 6:865, 2002.
171. H. Jin, H. Qiu, Y. Sakamoto, P. Shu, O. Terasaki, and S. Che. Mesoporous silicas by self-assembly of lipid molecules: Ribbon, hollow sphere, and chiral materials. *Chemistry - A European Journal*, 14:6413, 2008.
172. J. V. Selinger, M. S. Spector, and J. M. Schnur. Theory of self-assembled tubules and helical ribbons. *Journal of Physical Chemistry B*, 105(30):7157, 2001.
173. R. L. B. Selinger, J. V. Selinger, A. P. Malanoski, and J. M. Schnur. Shape selection in chiral self-assembly. *Physical Review Letters*, 93(15):158103, 2004.
174. G. Bellesia, M. V. Fedorov, and E. G. Timoshenko. Structural transitions in model beta-sheet tapes. *Journal of Chemical Physics*, 128:195105, 2008.
175. M. Bowick, M. Falcioni, and G. Thorleifsson. Numerical observation of a tubular phase in anisotropic membranes. *Physical Review Letters*, 79(5):885, 2007.
176. X. J. Xing and L. Radzihovsky. Phases and transitions in phantom nematic elastomer membranes. *Physical Review E*, 71(1):011802, 2005.
177. O. Stenull. Anomalous elasticity in nematic and smectic elastomer tubule phases. *Physical Review E*, 78(3):031704, 2008.
178. O. G. Schmidt, Ch. Deneke, S. Kiravittaya, R. Songmuang, H. Heidemeyer, Y. Nakamura, R. Zapf-Gottwick, C. Mller, and N. Y. Jin-Phillipp. Self-assembled nanoholes, lateral quantum-dot molecules, and rolled-up nanotubes. *IEEE Journal of Selected Topics in Quantum Electronics*, 8(5), 2002.
179. B. Schmidt. Minimal energy configurations of strained multi-layers. *Calculus of Variations*, 30:477, 2007.
180. T. D. Nguyen and S. C. Glotzer. Tunable spiral scrolls formed by laterally tethered rods. *preprint*.
181. F. S. Bates and G. H. Fredrickson. Block copolymer thermodynamics: Theory and experiment. *Annual Review of Physical Chemistry*, 41:525, 1990.
182. A. P. Alivisatos, K. P. Johnsson, X. Peng, T. E. Wilson, C. J. Loweth, M. P. Bruchez Jr, and P. G. Schultz. Organization of nanocrystal molecules using dna. *Nature*, 382:609, 1996.
183. S. Park, J. H Lim, S. W. Chung, and C. A. Mirkin. Self-assembly of mesoscopic metal-polymer amphiphiles. *Science*, 303:348, 2004.
184. J. H. Ryu and M. Lee. Liquid crystalline assembly of rodcoil molecules. *Structure and Bonding*, 128:63, 2008.

185. D. H. Gracias, V. Kavthekar, J. C. Love, K. E. Paul, and G. M. Whitesides. Fabrication of micrometer-scale, patterned polyhedra by self-assembly. *Advanced Materials*, 15:235, 2002.
186. J. C. Nelson, J. G. Saven, J. S. Moore, and P. G. Wolynes. Solvophobic driven folding of nonbiological oligomers. *Science*, 277(5333):1793, 1997.
187. J. Borg, M. H. Jensen, K. Sneppen, and G. Tiana. Hydrogen bonds in polymer folding. *Physical Review Letters*, 86(6):1031, 2001.
188. J. P. Kemp and Z. Y. Chen. Formation of helical states in wormlike polymer chains. *Physical Review Letters*, 81(18):3881, 1998.
189. R. A. Bertsch, N. Vaidehi, S. I. Chan, and W. A. Goddard III. Kinetic steps for alpha-helix formation. *Proteins: Structure, Function, and Genetics*, 33:343, 1998.
190. S. N. Fejer and D. J. Wales. Helix self-assembly from anisotropic molecules. *Physical Review Letters*, 99:086106, 2007.
191. S. Kim, S. Jeon, W. C. Jeong, H. S. Park, and S. Yang. Optofluidic synthesis of electroresponsive photonic janus balls with isotropic structural colors. *Advanced Materials*, 20:41294134, 2008.
192. Y. Yin and Y. Xia. Self-assembly of spherical colloids into helical chains with well-controlled handedness. *Journal of American Chemical Society*, 125(8):2048, 2003.
193. R. R. Price, W. J. Dressick, and A. Singh. Fabrication of nanoscale metallic spirals using phospholipid microtubule organizational templates. *Journal of American Chemical Society*, 125:11259, 2003.
194. J. P. Kemp and Z. Y. Chen. Helical structures in proteins. *Biomacromolecules*, 2:389, 2001.
195. S. A. Sabeur, F. Hamdache, and F. Schmid. Kinetically driven helix formation during the homopolymer collapse process. *Physical Review E*, 77:020802, 2008.
196. W. Helfrich and J. Prost. Intrinsic bending force in anisotropic membranes made of chiral molecules. *Physical Review A*, 38:3065–3068, 1988.
197. D. S. Chung, G. B. Benedek, F. M. Konikoff, and J. M. Donovan. Elastic free energy of anisotropic helical ribbons as metastable intermediates in the crystallization of cholesterol. *Proc. Natl. Acad. Sci. U.S.A.*, 90:11341–11345, 1993.
198. R. Oda, I. Huc, M. Schmutz, S. J. Candau, and F. C. MacKintosh. Tuning bilayer twist using chiral counterions. *Nature*, 399:566–569, 1999.
199. J. V. Selinger and J. M. Schnur. Theory of chiral lipid tubules. *Physical Review Letters*, 71:40914094, 1993.

200. Y. Guo, Y. Ma, L. Xu, J. Li, and W. Yang. Conformational change induced reversible assembly/disassembly of poly-l-lysine-functionalized gold nanoparticles. *Journal of Physical Chemistry C*, 111(26):9172–9176, 2007.
201. H. Shao and J. R. Parquette. Controllable peptidedendron self-assembly: Interconversion of nanotubes and fibrillar nanostructures. *Angewandte Chemie International Edition*, 48:2525–2528, 2009.
202. Y. Lim, K.-S. Moon, and Lee M. Recent advances in functional supramolecular nanostructures assembled from bioactive building blocks. *Chemical Society Reviews*, 38:925, 2009.
203. A. Sun and J. Lahann. Dynamically switchable biointerfaces. *Soft Matter*, 5:1555–1561, 2009.
204. C. Fernyhough, A. J. Ryan, and G. Battaglia. pH controlled assembly of a polybutadiene-poly(methacrylic acid) copolymer in water: packing considerations and kinetic limitations. *Soft Matter*, 5(8):1674–1682, 2009.
205. Q. Zhou, T. Chen, J. Zhang, L. Wana, P. Xie, C. C. Han, S. Yan, and R. Zhang. Hierarchical self-assembly of p-terphenyl derivative with dumbbell-like amphiphilic and rod-coil characteristics. *Tetrahedron Letters*, 49:5522–5526, 2008.
206. R. Kieffer, M. Prehm, K. Pelz, U. Baumeister, F. Liu, H. Hahn, H. Lang, G. Ungar, and C. Tschierske. Siloxanes and carbosilanes as new building blocks for t-shaped bolaamphiphilic lc molecules. *Soft Matter*, 5:1214–1227, 2009.
207. A. J. Crane, F. J. Martnez-Veracoechea, F. A. Escobedo, and E. A. Miller. Molecular dynamics simulation of the mesophase behaviour of a model bolaamphiphilic liquid crystal with a lateral flexible chain. *Soft Matter*, 4(9):1820–1829, 2008.
208. A. J. Schultz, C. K. Hall, and J. Genzer. Computer simulation of copolymer phase behavior. *Journal of Chemical Physics*, 117(22):10329–10338, 2002.
209. A. Jayaraman and K. S. Schweizer. Structure and assembly of dense solutions and melts of single tethered nanoparticles. *Journal of Chemical Physics*, 128(16):164904–13, 2008.
210. J. K. Kim, E. Lee, M. C. Kim, E. Sim, and M. Lee. Reversible transformation of helical coils and straight rods in cylindrical assembly of elliptical macrocycles. *Journal of American Chemical Society*, 131:17768–17770, 2009.
211. K. Chockalingam, M. Blenner, and S. Banta. Design and application of stimulus-responsive peptide systems. *Protein Engineering, Design and Selection*, 20:155–161, 2007.
212. J. Lin, G. Zhu, X. Zhu, S. Lin, T. Nose, and W. Ding. Aggregate structure change induced by intramolecular helix-coil transition. *Polymer*, 49:1132–1136, 2008.

213. K. E. Gebhardt, S. Ahn, G. Venkatachalam, and D. A. Savin. Rod-sphere transition in polybutadiene-poly(l-lysine) block copolymer assemblies,. *Langmuir*, 23:2851–2856, 2007.
214. K. E. Gebhardt, S. Ahn, G. Venkatachalam, and D. A. Savin. Role of secondary structure changes on the morphology of polypeptide-based block copolymer vesicles. *Journal of Colloid and Interface Science*, 317:70–76, 2008.
215. Z. Ahmed, N. S. Myshakina, and S. A. Asher. Dependence of the amiiip proline raman band on peptide conformation. *Journal of Physical Chemistry B*, 113(32):11252–11259, 2009.
216. S. S. Chang, C. W. Shih, C. D. Chen, W. C. Lai, and C. R. Chris Wang. The shape transition of gold nanorods. *Langmuir*, 15:701–709, 1999.
217. J. W. Yoo and S. Mitragotri. Polymer particles that switch shape in response to a stimulus. *Proceedings of the National Academy of Sciences of the United States of America*, 107:11205–11210, 2010.
218. Z. Yang, W. T. S. Huck, S. M. Clarke, A. R. Tajbakhsh, and E. M. Terentjev. Shape-memory nanoparticles from inherently non-spherical polymer colloids. *Nature*, 4:486–490, 2005.
219. P. Nolte, A. Stierle, N. Y. Jin-Phillipp, T. U. Schulli, and H. Dosch. Shape changes of supported rh nanoparticles during oxidation and reduction cycles. *Science*, 321:1654–1658, 2008.
220. R. G. Larson. *The structure and rheology of complex fluids*. Oxford University Press, 1999.
221. A. S. Keys, C. R. Iacovella, and S. C. Glotzer. Characterizing structure through shape matching and applications to self-assembly. *Annual Review of Condensed Matter Physics*, 2:263–285, 2011.
222. T. D. Nguyen, E. Jankowski, and S. C. Glotzer. Self-assembly and reconfigurability of shape-shifting particles. *preprint*.
223. J. Bishop, S. Burden, E. Klavins, R. Kreisberg, W. Malone, N. Napp, and T. Nguyen. Self-organizing programmable parts. *International Conference on Intelligent Robots and Systems*, 2005.
224. E. Klavins. Programmable self-assembly. *IEEE Control System Magazine*, 27(4):43–56, 2007.
225. E. Klavins, R. Ghrist, and D. Lipsky. A grammatical approach to self-organizing robotic systems. *IEEE Transactions on Automatic Control*, 51(6):949–962, 2006.
226. M. J. Vlot, J. Huinink, and J. P. van der Eerden. Design principles for self-assembly with short-range interactions. *Journal of Chemical Physics*, 110:55–61, 1999.

227. E. G. Noya, M. M. Conde, and C. Vega. Computing the free energy of molecular solids by the einstein molecule approach: Ices xiii and xiv, hard-dumbbells and a patchy model of proteins. *Journal of Chemical Physics*, 129:104704–16, 2008.
228. E. Jankowski and S. C. Glotzer. A comparison of new methods for generating energy-minimizing configurations of patchy particles. *Journal of Chemical Physics*, 131:104104, 2009.
229. S. Hwang, T. D. Nguyen, S. C. Glotzer, and J. Lahann. Directed assembly of biphasic magnetic particles. *preprint*.
230. A. Perro, S. Reculosa, S. Ravaine, E. Bourgeat-Lami, and E. Duguet. Design and synthesis of janus micro- and nanoparticles. *Journal of Materials Chemistry*, 15:3745–3760, 2005.
231. S. K. Smoukov, S. Gangwal, M. Marquez, and O. D. Velev. Reconfigurable responsive structures assembled from magnetic janus particles. *Soft Matter*, 5:1285–1292, 2009.
232. K. P. Yuet, D. K. Hwang, R. Haghgooie, and P. S. Doyle. Multifunctional superparamagnetic janus particles. *Langmuir*, 26(6):42814287, 2010.
233. E. G. Noya, C. Vega, J. P. K. Doye, and A. A. Louis. The stability of a crystal with diamond structure for patchy particles with tetrahedral symmetry. *Journal of Chemical Physics*, 132:234511–13, 2010.
234. Q. Chen, S. C. Bae, and S. Granick. Directed self-assembly of a colloidal kagome lattice. *Nature*, 469:381, 2011.
235. F. Sciortino, E. Bianchi, J. F. Douglas, and P. Tartaglia. Self-assembly of patchy particles into polymer chains: A parameter-free comparison between wertheim theory and monte carlo simulation. *Journal of Chemical Physics*, 126(19):194903, 2007.
236. R. Fantoni, D. Gazzillo, A. Giacometti, M. A. Miller, and G. Pastore. Patchy sticky hard spheres: analytical study and monte carlo simulations. *Journal of Chemical Physics*, 127(23):234507, 2007.
237. W. L. Miller and A. Cacciuto. Hierarchical self-assembly of asymmetric amphiphatic spherical colloidal particles. *Physical Review E*, 80:021404–6, 2009.
238. S. Jiang, Q. Chen, M. Tripathy, E. Luijten, K. S. Schweizer, and S. Granick. Janus particle synthesis and assembly. *Advanced Materials*, 22:1060–1071, 2010.
239. M. Lattuada and T. A. Hatton. Preparation and controlled self-assembly of janus magnetic nanoparticles. *Journal of the American Chemical Society*, 129(42):1287812889, 2007.
240. A. Walther and A. H. E. Muller. Janus particles. *Soft Matter*, 4:663–668, 2008.

241. Z. L. Zhang, A. S. Keys, T. Chen, and S. C. Glotzer. Self-assembly of patchy particles into diamond structures through molecular mimicry. *Langmuir*, 25:11547–11551, 2005.
242. C. R. Iacovella, A. S. Keys, and S. C. Glotzer. Self assembly of soft matter quasicrystals and their approximants. *arXiv:1102.5589v1 [cond-mat.soft]*, 2011.
243. J. Q. Cui and I. Kretzschmar. Surface-anisotropic polystyrene spheres by electroless deposition. *Langmuir*, 22:8281–8284, 2006.
244. D. Zerrouki, J. Baudry, D. Pine, P. Chaikin, and J. Bibette. Chiral colloidal clusters. *Nature*, 455(18):380, 2008.
245. V. N. Manoharan, M. T. Elsesser, and D. J. Pine. Dense packing and symmetry in small clusters of microspheres. *Science*, 301:483487, 2003.
246. C. E. Snyder, A. M. Yake, J. D. Feick, and D. Velegol. Nanoscale functionalization and site-specific assembly of colloids by particle lithography. *Langmuir*, 21:48134815, 2005.
247. J. Kolafa and I. Nezbeda. Monte carlo simulations on primitive models of water and methanol. *Molecular Physics*, 61:161–175, 1987.
248. C. De Michele, S. Gabrielli, P. Tartaglia, and F. Sciortino. Dynamics in the presence of attractive patchy interactions. *Journal of Physical Chemistry B*, 110:8064, 2006.
249. E. Bianchi, P. Tartaglia, E. Zaccarelli, and F. Sciortino. Theoretical and numerical study of the phase diagram of patchy colloids: ordered and disordered patch arrangements. *Journal of Chemical Physics*, 128:144504, 2008.
250. J. M. Tavares, P. I. C. Teixeira, and M. M. Telo da Gama. Criticality of colloids with distinct interaction patches: The limits of linear chains, hyperbranched polymers, and dimers. *Physical Review E*, 80:021506, 2009.
251. D. C. Rapaport, J. E. Johnson, and J. Skolnick. Supramolecular self-assembly: Molecular dynamics modeling of polyhedral shell formation. *Computer Physics Communications*, 121122:231235, 1999.
252. D. C. Rapaport. Self-assembly of polyhedral shells: A molecular dynamics study. *Physical Review E*, 70:051905–13, 2004.
253. H. D. Nguyen, V. S. Reddy, and C. L. Brooks III. Deciphering the kinetic mechanism of spontaneous self-assembly of icosahedral capsids. *Nano Letters*, 7(2):338–344, 2007.
254. D. C. Rapaport. Studies of reversible capsid shell growth. *Journal of Physics: Condensed Matter*, 22:104115–6, 2010.
255. A. W. Wilber, J. P. K. Doye, A. A. Louis, and A. C. F. Lewis. Monodisperse self-assembly in a model with protein-like interactions. *arXiv:0907.4811v1*, 2009.

256. A. W. Wilber, J. P. K. Doye, and A. A. Louis. Self-assembly of monodisperse clusters: Dependence on target geometry. *Journal of Chemical Physics*, 131:175101–13, 2009.
257. G. Villar, A. W. Wilber, A. J. Williamson, P. Thiara, J. P. K. Doye, A. A. Louis, M. N. Jochum, A. C. F. Lewis, and E. D. Levy. The self-assembly and evolution of homomeric protein complexes. *arXiv:0811.3716v1*, 2008.
258. R. P. Sear. Phase behavior of a simple model of globular proteins. *Journal of Chemical Physics*, 111(10):4800–4806, 1999.
259. X. Li, J. D. Gunton, and A. Chakrabarti. A simple model of directional interactions for proteins. *Journal of Chemical Physics*, 131:115101–8, 2009.
260. C. Gogelein, G. Ngele, R. Tuinier, T. Gibaud, A. Stradner, and P. Schurtenberger. A simple patchy colloid model for the phase behavior of lysozyme dispersions. *Journal of Chemical Physics*, 129:085102–12, 2008.
261. P. Tarazona. Free-energy density functional for hard spheres. *Physical Review A*, 31:2672–2679, 1985.
262. G. L. Aranovich and M. D. Donohue. Modeling self-assembly in molecular fluids. *Journal of Chemical Physics*, 116:7255, 2002.
263. A. B. Pawar and I. Kretzschmar. Fabrication, assembly, and application of patchy particles. *Macromolecular Rapid Communications*, 31:150–168, 2010.